# Atomically dispersed Co-Mn dual sites anchored in photoresponsive carbon nitride mediated peroxymonosulfate activation for elimination of petroleum hydrocarbon in water

Qi Guo [a], Xue-Fang Yu [b,*], Kaisheng Zhang [c,*], Linhong Xia [a], Senmiao Liu [a], Weilong Zhang [a], Yujie Du [a], Hua Tang [d], Yanhua Peng [a], Zhuo Li [a], Liqin Duan [e], Xiaolong Yang [a,*,1]

[a] School of Chemistry and Chemical Engineering, State Key Laboratory of Bio-fibers and Eco-textiles, Collaborative Innovation Center of Shandong Marine Bio-based Fibers and Ecological textiles, Qingdao University, 308 NingXia Road, Qingdao 266071, PR China
[b] The Laboratory of Theoretical and Computational Chemistry, School of Chemistry and Chemical Engineering, Yantai University, No. 32 Qingquan Road, Yantai 264005, PR China
[c] Environmental Materials and Pollution Control Laboratory, Institute of Solid State Physics, HFIPS, Chinese Academy of Sciences, Hefei 230031, PR China
[d] School of Environmental Science and Engineering, Qingdao University, Qingdao 266071, PR China
[e] Key Laboratory of Marine Ecology and Environmental Sciences, Institute of Oceanology, Chinese Academy of Sciences, Qingdao 266071, PR China

## ARTICLE INFO

## ABSTRACT

The atomic dispersed heterogeneous catalysts are attracting much research interests. Recently, multiple active sites (two, three or even more) exhibits all-round characters for regulation of intrinsic active sites. However, depth exploration of multiple active sites in persulfate activation etc fenton-like advanced oxidation process is still in its infancy. Herein, binary atomic dispersed active sites anchored in visible-light-responsive carbon nitride Co-Mn/CN catalyst was designed representatively. The characterization and theory calculation clarified the coordination environment of metallic center atoms and confirms its CoN4-MnN2 moiety. The unique coordinated geometry on the one hand highlights the synergy effect between photocatalysis and peroxymonosulfate (PMS) activation, on the other hand promotes the form of metastable metal-PMS complex and subsequent activation process. Furthermore, the catalysts present efficient application to purify the oil spill pollutes water considering water quality, pH and durability etc. This work sheds light on the rational regulation of diatomic sites in photo-Fenton-like catalysts.

## 1. Introduction

Petroleum resources transported over the whole world by waterways put the oil spills and oil seepage at risk. Petroleum hydrocarbons leaked into the water area have detrimental impact on water body and human beings' ecosystem, which is lingering and profound [1]. Unfortunately, although oil spill accidents occur in different areas every year, the remediation technology for oil spill pollution has not been continuously developed and innovated, basically still staying at the original level [2–4].

Recently, advanced oxidation process based on persulfate (PS-AOPs) attracted extensive attention for environmental emergency pollutants degradation because of its high redox potential ($E^0(SO_4^{\bullet-}/SO_4^{2-})$= 2.6–3.1 $V_{NHE}$, $\tau_{1/2\ SO4\bullet}$= 30–40 μs, $E^0(\bullet OH/OH^-)$= 1.9–2.7 $V_{NHE}$ , $\tau_{1/2\ \bullet OH} <=$

1 μs) as well as broad applicable conditions (reactive species of non-radical path is less affected by environmental conditions including metastable persulfate/catalyst complexes, singlet oxygen ($^1O_2$), and high-valent metals) [5]. Transition metals (e.g., Fe, Co, Mn, Ni, and Cu) have been widely studied to activate PS [6–10] to produce reactive species due to their low energy requirement and high efficiency. Among them, heterogenous Cobalt active sites exhibits superior adsorption and activation of PMS because of pristine specific 3d band structure of $Co^{2+}$ and suitable redox potential (1.82 eV) [11,12]. However, sluggish PS activation kinetics as well as obstructive electron transfer path between PS and catalyst still hampers the atomic utilization efficiency.

Single-atom catalysts (SACs) attracts numerous research interests in heterogenous activation of PS because of maximum active sites utilization efficiency and excellent modulation of metal-ligand coordination

* Corresponding authors.
  *E-mail addresses:* yuxuefang2008@gmail.com (X.-F. Yu), kszhang@iim.ac.cn (K. Zhang), yangxl@qdu.edu.cn (X. Yang).
  [1] https://orcid.org/0000-0001-6317-724X

moiety [13–17]. Liu et al. firstly devised CoN₄ SACs for degradation of recalcitrant organics via activation of PMS, they claimed Co atom is responsible for PMS activation and adjacent pyrrolic N sites tend to adsorbs pollutant molecules [18]. Zhan group and Xu group independently regulated the $^1O_2$ species generation path over $CoN_{2+2}$ active site and $Co-N_3O_1$ moiety in PMS activation, respectively, which presents superior performance for removal of environmental pollutants [19,20].

Hitherto, tremendous efforts have been contributed to modulate electronic structure of center atom as well as corresponding coordination structure. However, persulfate-based Fenton-like process is considered as typical multistep reaction related with adsorption, activation and desorption steps. Sole single atom site cannot simultaneously
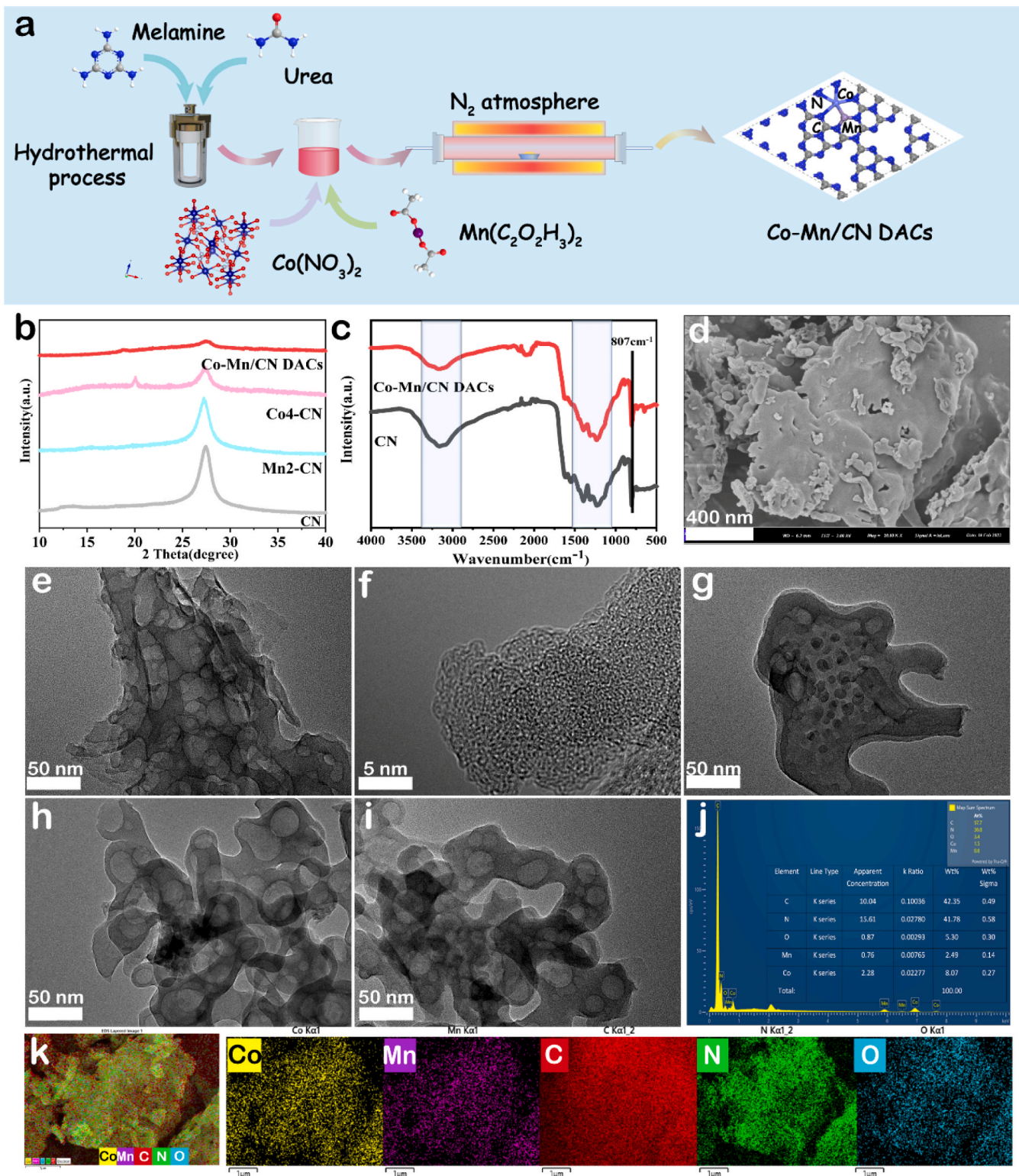


**Fig. 1.** (a) Synthesized route for Co-Mn/CN DACs; (b) XRD; (c) FTIR; FE-SEM images of (d) Co-Mn/CN DACs; TEM images of (e) Co-Mn/CN DACs, (g) CN, (h) Co4-CN and (i) Mn2-CN; HRTEM images of (f) Co-Mn/CN DACs; EDS results (j) and elemental mapping (k) of Co-Mn/CN DACs.

satisfy the adsorption of PMS and pollutants, as well as the subsequent free radical generation process, which result in sluggish reaction kinetics [14]. Compared with sole metal active sites, the coexistence of multiple metal active site will greatly promote the activation kinetics of PMS in the way of tandem catalysis. Recently, dual-atom-site or few-atom-site catalysts with two or more atoms bonded to each other or dispersed randomly gain extensive research interests from a series of key reactions related to energy and environment, such as ORR (oxygen reduction reaction), OER (oxygen evolution reaction), $CO_2$ RR ($CO_2$ reduction reaction), Nitrate Reduction, Fischer−Tropsch Synthesis, Fenton-like reaction and chemical synthesis et al. [14,21–24]. The neighboring two or few atoms possess substantially different electronic structure and coordination environment, which make it possible to adjust the d-band center of metal active site and thereafter optimize the adsorption behavior of intermediates [25,26]. He group found $FeCoN_6$ configuration and pyrrolic N in Fe-Co/N-doped carbon DACs tend to facilitate adsorption of target molecules and further shorten migration distance between ROS and adsorbed intermediate [27]. Zhou group proposed Fe atom in Fe-Co/N-C DACs tend to transfer electron to adjacent Co atom and up shift its d-band center, thus facilitating adsorption and decomposition kinetics of PMS [14]. Manganese presents variable valence states of $Mn^{2+}/Mn^{3+}/Mn^{4+}$, which is accompanied by electron transfer process and plays a role in promoting the redox reaction. In addition, manganese metal has a large amount of cheap and low environmental pollution, so it has inherent advantage to cooperate with Co SACs catalyst in sewage treatment [28]. Nevertheless, exploration of DACs in PMS activation process still in its in infancy and identification of PMS adsorption sites, activation active sites and intrinsic mechanism of PMS activation remains ambiguous. Furthermore, few atom catalysts provide unparalleled opportunity to current photocatalysis, which possess natural-born capability of breaking O-O bond of PMS [29–31].

Herein, we report Co-Mn/CN DACs as superior Fenton-like catalysts for remediation of petroleum hydrocarbon polluted water via activation of PMS with or without illumination. XAFs analysis demonstrates coordination environment of center atoms and confirms the Co1-N4O3-Mn1 moiety in Co-Mn/CN DACs. DFT calculation indicates the Co and Mn prefer to bond together, and they tend to coordinate with four and two N atoms, respectively. The optimized Co-Mn/CN DACs could strongly adsorb and decompose PMS efficiently, and eventually leading to the generation of radicals as well as non-radicals like $^1O_2$. Thus, Co-Mn/CN DACs exhibited superior catalytic degradation activity for aqueous $C_{14}H_{30}$ no matter in deionized water or real natural seawater. Excellent durability as well as applicable broad pH value further promote the possibility of practical application. Finally, the activation mechanism for PMS over DACs were illustrated based on experiments and DFT calculations. This work gives first insights to dual Co-Mn atom-planted g-$C_3N_4$ substrate with binary active sites for round-the-clock elimination of petroleum hydrocarbon in water.

## 2. Experimental section

### 2.1. Sample preparation

The synthesized route of Co-Mn/CN DACs is illustrated in Fig. 1a. Briefly, a certain amount of urea and melamine was dissolved in deionized water. The mixed solution was poured into a 100 mL Teflon autoclave and self-assembled at 180 °C for 24 h. The product was washed and dried. Then, precursors above mentioned, $Co(NO_3)_2 \cdot 6H_2O$ and $C_4H_6O_4Mn$ was added to deionized water and keep stirring for 8 h. The resulted products after dry were placed in a corundum porcelain boat with a lid and heated to 500 °C at 2.5 °C/min in nitrogen atmosphere for 4 h. The resulting sample is marked as Co-Mn/CN DACs. The concrete method other catalysts were prepared were recorded in SI. Text S1.1, 1.2.

### 2.2. Characterization

XRD was carried out by Smart Lab 3KW (Rigakum, Japan) with Cu Kα (λ = 0.15418 nm). The metal content was determined by ICP-MS (Aglient, USA). The FT-IR spectrum was detected by Nicolet is 50 (Thermo, USA). The SEM images were recorded by Hitachi SU8010 (JOEL, Japan), and the microscopic morphology was collected by Regulus8100 (Hitachi, Japan) FESEM. TEM, HRTEM and corresponding elemental mapping were performed at 300 kV on JEM 2100F (JEOL, Japan) operating. XPS were conducted by ESCALAB Xi+(Thermo Fisher) with Al Kα (hν = 1486.6 eV) and standard carbon is employed for calibration. The UV-Vis DRS were measured by SPECORD 210 PLUS spectrophotometer with $BaSO_4$ reference. Steady-state and transient photoluminescence (PL) spectroscopy (room temperature, Excitation wavelength at 365 nm) was performed with Edinburgh FLS1000. Photoelectrochemical results were measured by electrochemical workstation (ChenHua, China) by three-electrode method. In situ-ESR spectra were recorded with Bruker model A300 spectrometer with 300 W Xe lamp. XAFS spectra were measured at the beamline 1W1B station of the Beijing synchrotron Radiation Facility (BSRF) and BL11B station in the Shanghai Synchrotron Radiation Facility (SSRF), China.

### 2.3. Photocatalytic petroleum hydrocarbon degradation reaction

n-tetradecane ($C_{14}H_{30}$) was used to simulate the photocatalytic degradation of petroleum hydrocarbons. The experiment was carried out in a jacketed quartz reactor, and the circulating condensing device maintained the reaction temperature in the reactor. About 100 mg photocatalyst, 20 mg C14 and 10 mL deionized water were added to the reactor. After continuous stirring for 30 min to reach the adsorption-desorption equilibrium, a certain dose of PMS is added. Using 300 W Xenon lamp (PLS-SXE300) and 420 nm cut-off filter to ensure visible light, irradiation reaction system for 2 h. After the reaction, the mixture was separated by extraction of dichloromethane ($CH_2Cl_2$). Gas chromatography (HP-5, Kejie 1100 A, China) was used for quantification with n-decane ($C_{10}H_{22}$) as internal standard. Details of experimental section is recorded in Text. S1.4.

## 3. Results and discussion

### 3.1. Structural characterization

The morphologies of original CN, Co4-CN, Mn2-CN and Co-Mn/CN DACs were observed by SEM (Fig. 1d and Fig. S1) and TEM (Fig. 1e-1i). CN exhibits nanosphere-like cluster contour profile as shown in Fig. 1g and there are many independent blowholes inside. The same bubble-like structure is also observed in single Co, Single Mn and binary Co-Mn embedded samples (Figs. 1h, 1i). It should be noted that the frame of CN change from no-cluster to square-like sheet for Co-Mn/CN DACs samples as shown in Fig. 1d, which could be attribute to the presence of metal precursor prevents the thermal condensation of supermolecule precursor. Dark field TEM showed that metal was successfully incorporated into the material (Fig. S2). Deeply, compared with CN (Fig. S3), it is hard to found the lattice fringe of $CoO_x$ and $MnO_x$ phase in binary metal Co-Mn/CN DACs samples (Fig. 1f), which implies the high dispersion characteristic of Co and Mn species [32]. Such superior metal species dispersity could also be testified by SEM-EDS mapping as shown in Fig. 1j , 1k, Co, Mn, C, N and O elements dispersed uniformly over the square-like Co-Mn/CN DACs sample. No large clusters or nanoparticles of metal species are found. According to EDS semi-quantitative analysis results, the metal ratios of cobalt and manganese in Co-Mn/CN DACs were 7.49 and 3.18 wt%, respectively, which was consistent with the ICP-MS results (7.71 and 3.43 wt%).

The crystal phase was determined by XRD (Fig. 1b). Double major characteristic diffraction peaks were observed in CN at 13° and 27.5°, which is ascribed to in-plane heptazine repeating units of (100) facet as

well as interlayer long distance ordered arrangement of (002) facets of graphitic carbon nitride [33,34], respectively. The introduction of binary metal species would greatly disturb the ordered characteristics of above-mentioned CN. Specifically, representative signals of (100) and (002) fades greatly and even disappear thoroughly for former one. Comparatively, diffraction signals of CN substrate tend to disappear and crystalline $CoO_x$ signal appears with the increase of Co amount for Cox-CN (Fig. S4). The introduction of Mn species apparently is conductive to suppress the crystallization process of $CoO_x$ (Fig. S5). However, the excessive amount of Mn species would promote the formation of Co-Mn spinel phase ($CoMn_2O_4$) [35]. The chemical functional groups of CN and Co-Mn/CN DACs were studied by FT-IR technique (Fig. 1c). The typical stretching modes of heterocyclic CN bonds locates between 1200 and 1650 $cm^{-1}$, breathing vibration mode of characteristic heptazine units of CN skeleton appears at 807 $cm^{-1}$, residual N-H bonds reside at 3199 $cm^{-1}$ due to incomplete polymerization, and the broad absorption bands at 3000–3500 $cm^{-1}$ originated from stretching mode of O–H [36–38]. The FTIR spectra of Co-Mn/CN DACs exhibit almost similar profile compare to CN, suggesting the main g-$C_3N_4$ structure are well remained in Co-Mn/CN DACs.

The surface elemental chemical states are rather important information for photocatalysis and PS activation process. The survey of XPS of Co-Mn/CN DACs testifies the presence of Co, Mn, C, N and surface adsorbed oxygen species, no other impurities is found (Fig. S6). Specifically, Co 2p of Co-Mn/CN DACs can be deconvoluted into three doublet peaks locate at 781.40 eV and 796.77 eV, 785.49 eV and 800.18 eV, 788.73 eV and 803.42 eV, corresponding to $Co^{3+}$, $Co^{2+}$ and satellite, respectively [20,39,40] (Fig. 2a, Table. S1). It should be noted that BE (Binding Energy) values of Co species in binary sample exhibit a shift to low BE direction compared to pristine Co4-CN catalyst (Fig. S7). On the other hand, Mn 2p comprise of peaks locate at 641.72 eV and 652.67 eV, 645.27 eV and 656.22 eV, 648.2 eV, assigning to $Mn^{2+}$, $Mn^{3+}$ and $Mn^{4+}$ (Fig. 2b, Table. S2), respectively. Correspondingly, BE values of Mn species in Co-Mn/CN DACs sample either exhibit an apparent shift to low BE direction compared to pristine Mn2-CN catalyst (Fig. S8). Such negative shift of BE value of Co and Mn in Co-Mn/CN DACs catalyst compared with single metal anchored metal-CN catalysts implies the change of surrounding coordination environments of metal. That is, the decrease of amount of surrounding adjacent ligands of Co, Mn and increase of probability of Co-Mn bonding is beneficial to
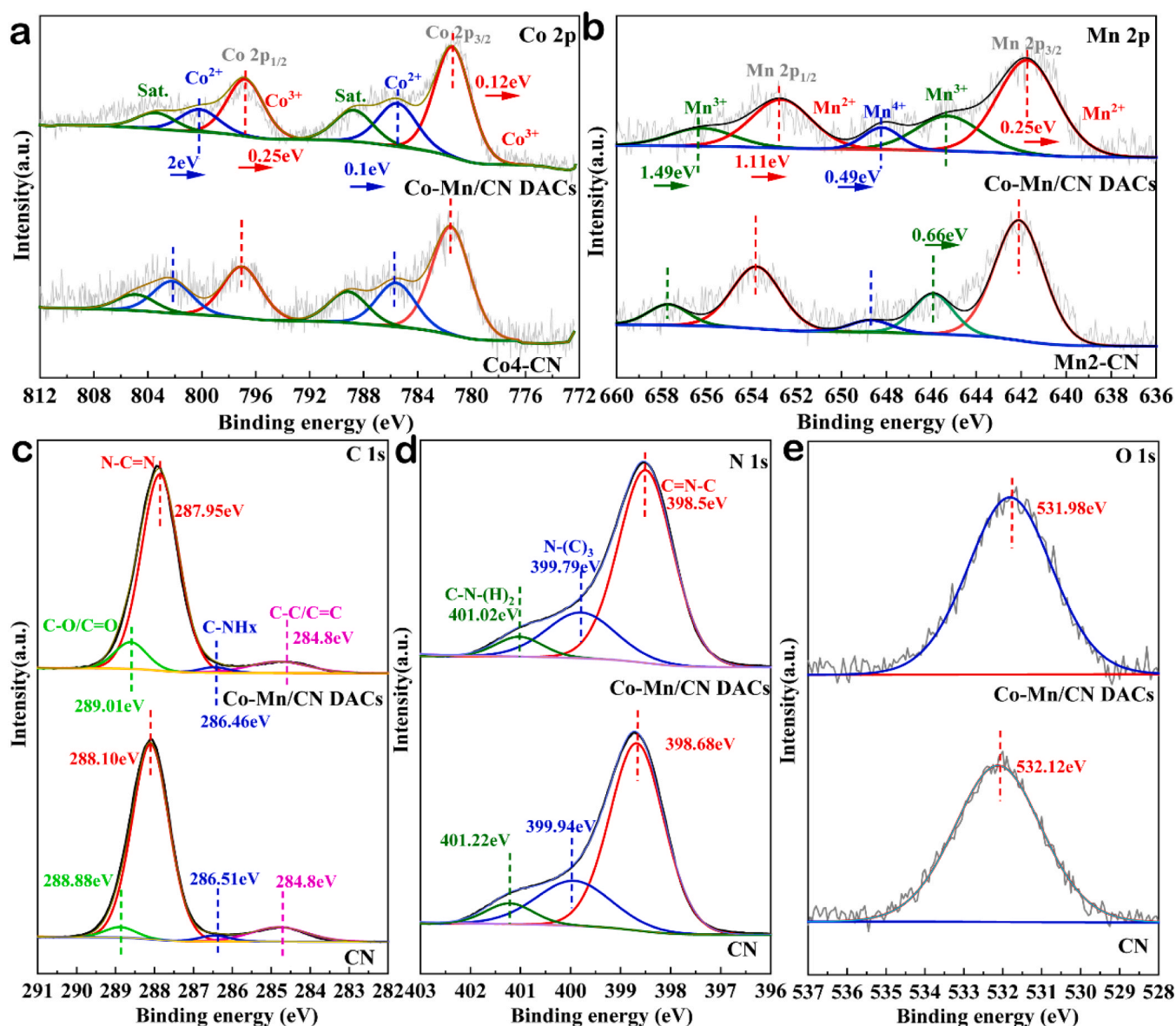


**Fig. 2.** XPS spectra of (a) Co 2p, (b) Mn 2p, (c) C 1 s, (d) N 1 s and (e) O 1 s for catalysts.

decrease of BE values. More importantly, the latter factor is much helpful for the synergistic cycle of binary metal for PMS activation path. The surface chemical states of carbon and nitrogen are also analyzed as shown in Figs. 2c, 2d. The core level of C1s of Co-Mn/CN DACs catalyst is divided into triplet peaks locates at 284.8, 286.46 and 287.95 eV, corresponding to standard carbon, –C–NH$_x$ amino carbon originated from uncomplete thermal-condensation of melem as well as pyridine carbon N–C≡N–, respectively (Fig. 2c). The core level of N1s of Co-Mn/CN DACs catalyst is splitted into three peaks located at 398.5, 399.8, 401.0 eV, assigning to pyridine nitrogen –C–N = C– groups, bridged N atoms N–(C)$_3$ and C–N–H (Fig. 2d), respectively. Furthermore, the BE values of C and N in Co-Mn/CN DACs almost remains the same as that of pristine CN, which suggests characteristic heptazine unit of g-C$_3$N$_4$ bulk structure was well remained. In addition, the "C-O/C≡O" BE value of Co-Mn/CN DACs is 0.16 eV lower than that of the original CN (Fig. 2e), and the N–C≡N species in Co-Mn/CN DACs are less than that in CN. Oxygen atom tend to replace two coordination sp2 hybridized N atoms in triazine rings [20,41]. Such replacement would alter configurational environment of Co atoms and change the electronic structure of Co-Mn/CN DACs further due to the difference of electronegativity.

The X-ray absorption near-edge structure (XANES) and extended X-ray absorption fine structure (EXAFS) analyses were carried out to explore electronic structure and local coordination environment of Co and Mn atoms in Co-Mn/CN DACs (Table. S3). The Co K-edge XANES profiles shown in Fig. 3a indicates that the valence of Co species in DACs is between +2 to +3, which is distinctly different from that of Co foil as well as CoO presented in inset of Fig. 3a. It is in consistent with the above Co 2p XPS results (Fig. 2a). In FT-EXAFS spectra, one major peak at approximately 2.1 Å is ascribed to typical first shell Co-Co pair. Co-Mn/CN DACs exhibits one major peak at 1.38 Å (Co-N), which is approximately to 1.47 Å of Co-O in first shell of Co$_3$O$_4$, no Co-Co bond peak is detected, confirming the absence of metal nanoparticles or clusters. indicating the existence of atomically dispersed Co-N sites. Simultaneously, Co-O as well as Co-Mn has been confirmed by small peaks located at 2.36 and 2.88 Å as shown in Fig. 3b. The quantitative least-squares EXAFS curve-fitting analysis were employed to confirm the coordination configurations of Co-Mn/CN DACs compared to Co foil and CoPc (Fig. 3c). The simulation reveals the coordination number for Co-N, Co-O and Co-Mn is determined to be 4.4, 3.0 and 1.4 with average bond lengths of 2.00 Å, 2.17 Å and 2.55 Å, respectively, indicating a single-atom Co-N$_4$O$_3$-Mn moiety. Furthermore, the Wavelet transformation analysis of EXAFS are conducted to discriminate backscattering atom and provide high resolution in K space as well as R space. As shown in Fig. 3d, Co-Mn/CN DACs exhibits distinct intensity maximum of 4.48 Å$^{-1}$, which is differently from the contour intensity maxima of
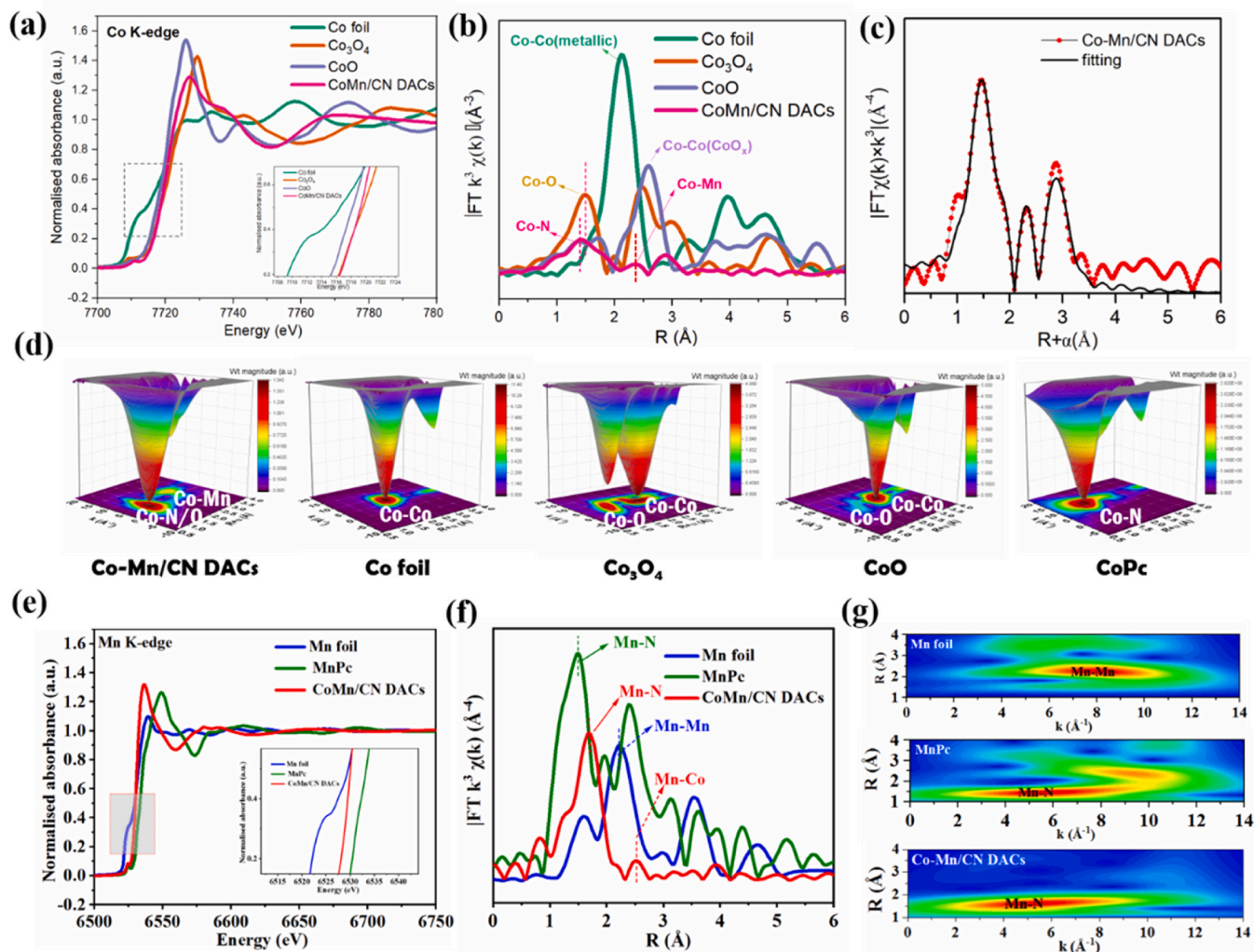


**Fig. 3.** (a) Normalized XANES spectra at the Co K-edge of Co-Mn/CN and reference sample including Co foil, Co$_3$O$_4$, CoO; (b) Co K-edge k$^3$-weighted FT-EXAFS spectrum of corresponding samples. Corresponding Fourier transforms (c) R space fitting results. Red: observed data; black: fitted data; (d) Co WT-EXAFS of Co-Mn CN catalysts and reference samples including Co foil, Co$_3$O$_4$, CoO and CoPc. (e) Mn K-edge normalized XANES spectra. (f) FT of the k$^3$-weighted EXAFS spectra. (g) WT of Mn foil, Mn Pc and Co-Mn/CN (from top to bottom).

other reference sample locating at 7.95 (Co foil), 7.21 (CoO), 6.53 ($Co_3O_4$) and 11.8 (CoPc), respectively. The WT EXAFS results states the appearance of heteronuclear centers of single atomic cobalt-manganese species. The Mn K-edge absorption-edge position of Co-Mn/CN DACs is between those of Mn foil and MnPc (Fig. 3e), and it is closer to the position of MnPc, implying that the Mn valance state approaches +2. Furthermore, the EXAFs of Mn demonstrates the presence of Mn-N bond (1.65 Å) (Fig. 3f), which is close to the characteristic Mn-N2 entity of MnPc and no Mn-Mn bond (2.24 Å) is observed. It suggests the atomically dispersion states of Mn species. Faint signal at 2.43 Å is reasonably assigned to Mn-Co bond [42], which is similar to results of Feng et al., they proposed Mn-Co (Co-Mn) bond length is fitted to be 2.49 ± 0.02 (2.47 ± 0.05) Å. The wavelet transforms (WT) contour plots (Fig. 3g) of Co-Mn/CN DACs implies the maximum intensity at 4.98 Å, which was associated to the Mn-N coordination bond [43]. Hence, taken together, the above EXAFS analysis results testified presence of atomically dispersed $Co1-N_4O_3-Mn1$ moiety.

## 3.2. Light-adsorption properties, carries' separation kinetic and PMS-catalyst photo-electron-chemical characterization

Light harvesting capability of samples are conducted by UV-Vis DRS technique. Characteristic optical absorption of CN ranges from 250 to 450 nm (intrinsic excitation of π-π* electron transition) (Fig. 4a). Limiting by inactivation of n-π* excitation, original g-$C_3N_4$ can only absorb light with wavelength lower than 460 nm. The introduction of cobalt species just perfectly makes up for insufficient light absorption of CN in the range greater than 460 nm. Apparent absorption signals range from 460 to 750 nm are observed for samples related with Co species like Co4-CN and Co-Mn/CN DACs. While the presence of manganese species does not affect light absorption capacity. The corresponding bandgap of catalysts were calculated by Tauc method (Fig. 4b). The $E_g$ are determined to be 2.87, 2.67, 2.82, 2.71 eV for CN, Co4-CN, Mn2-CN and Co-Mn/CN DACs, respectively. CB potential were calculated to be −1.0 eV and −1.18 eV respectively for CN and Co-Mn/CN DACs by VB-XPS results.

The current in the Co-Mn/CN DACs system in the LSV curve is
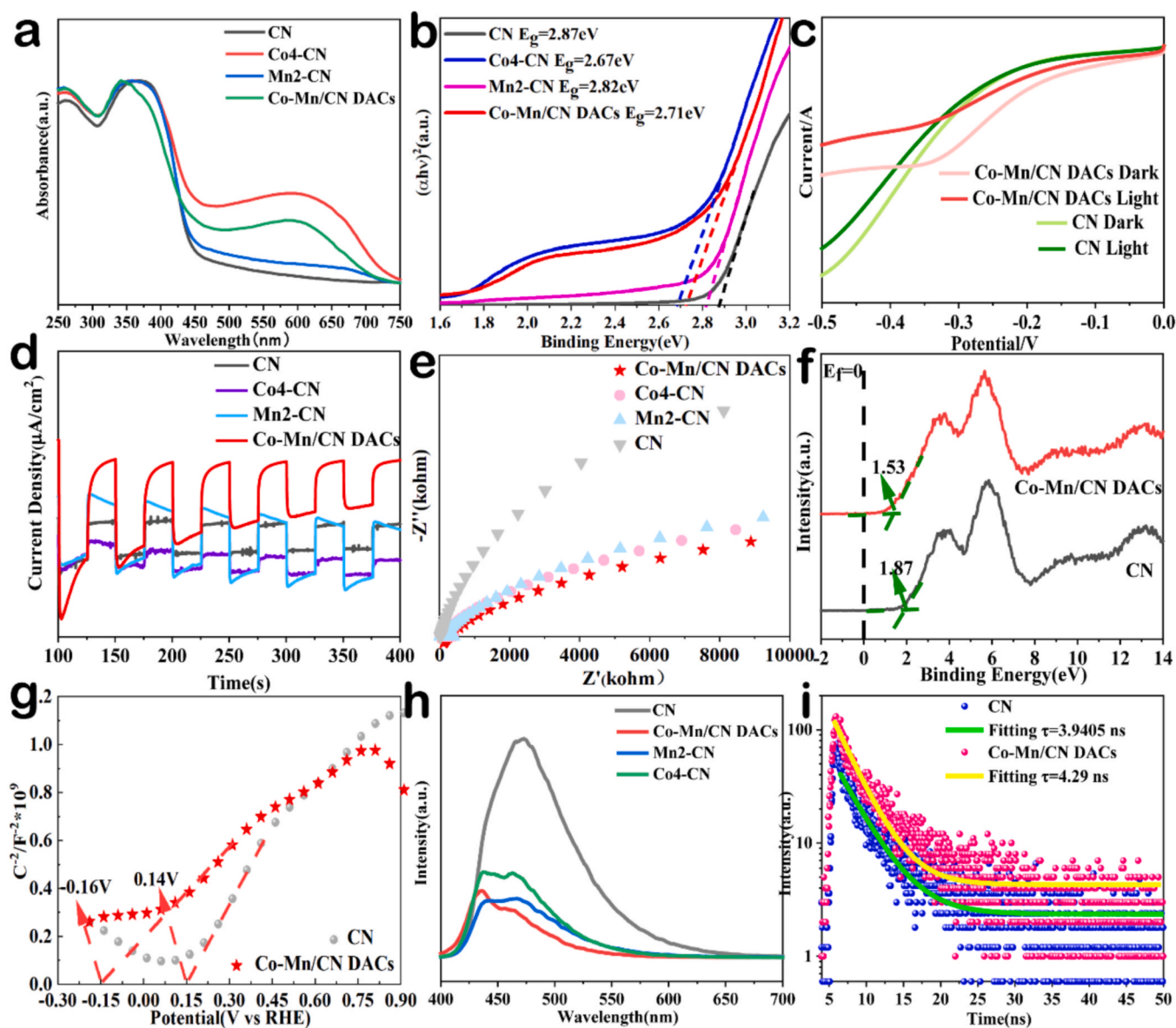


**Fig. 4.** (a) UV–vis DRS spectra (b) Tacu plots; (c) LSV; (d) Transient photocurrent (TPC) response; (e) EIS Nyquist plots; (f) VB-XPS spectra; (g) Mott-Schottky plots; (h) PL spectra; (i) TRPL spectra.

significantly stronger than that in bare CN, which further proves that Co-Mn/CN DACs has stronger electron transfer ability (Fig. 4c). The separation behavior of photo-induced electron-hole pairs is prerequisite for photocatalysis, and is either beneficial for the activation of PMS. The carriers' separation and transfer efficiency are evaluated by photo-electro-chemical performance. Binary Co-Mn/CN DACs exhibits the largest transient photocurrent intensity compared to its single counterpart in TPC experiment (Fig. 4d). Correspondingly, Co4-CN, Mn2-CN and Co-Mn/CN DACs catalyst all exhibits smaller impedance arc radius compared to its original substrates, which means the smallest charge-transfer resistance (Fig. 4e). The valence band positions of CN and Co-Mn/CN DACs are determined to be 1.87 eV and 1.53 eV, respectively (Fig. 4f). In addition, the introduction of metal sites modulated the electronic structure of CN, which drive the conduction band of Co-Mn/CN DACs shift negatively, and also causes the difference of Fermi level of the material (Fig. 4f, 4g). The recombination behavior of carriers is effectively suppressed in SSPL for Co-Mn/CN DACs, which is apparently weaker than that of CN, Co4-CN as well as Mn2-CN (Fig. 4h). It is well consistent with the above TPC as well as EIS results. The carriers' average lifetime is determined to be 3.9405 ns and 4.2933 ns for original CN and Co-Mn/CN DACs, much longer carriers' lifetime of Co-Mn/CN DACs indicates the superior separation and transfer kinetics of excitons (Fig. 4i).

Finally, the electron transfer process between catalyst with PMS is investigated by photo-electrochemical method as shown in Fig. 5. The optimal Co-Mn/CN DACs catalyst quickly showed a clear reverse current signal after injection into the PMS in ampere i-t curves compared to non-metal CN catalyst (Fig. 5a), confirming the effective transfer process of electrons from Co-Mn/CN DACs site to the PMS activator. In addition, the OCP signal of Co-Mn/CN DACs electrode significantly increased when PMS was added (Fig. 5b), which again testified enhancement of electron transfer process from Co-Mn/CN DACs site to PMS, and the surface potential of the catalyst is increased due to the partial electron transfer phenomenon of catalyst-PMS* species[44]. Correspondingly, Co-Mn-PMS signals (837 $cm^{-1}$) is also observed in In situ-Raman spectra shown in Fig. 5c, 5d, and the absence of O-O (882 $cm^{-1}$) and $HSO_5^-$ (1059 $cm^{-1}$) in DACs/PMS implies the consumption of PMS by DACs efficiently.

### 3.3. DACs activates PMS to degrade oil spill pollutes water

The catalytic degradation efficiency of original CN, single metal-CN as well as DACs are evaluated initially in a certain environment with or without visible light. The degradation performance increases as the amount of Cobalt precursor increases. Co4-CN exhibits the best degradation efficiency (~51 %) and excessive metal addition decreases
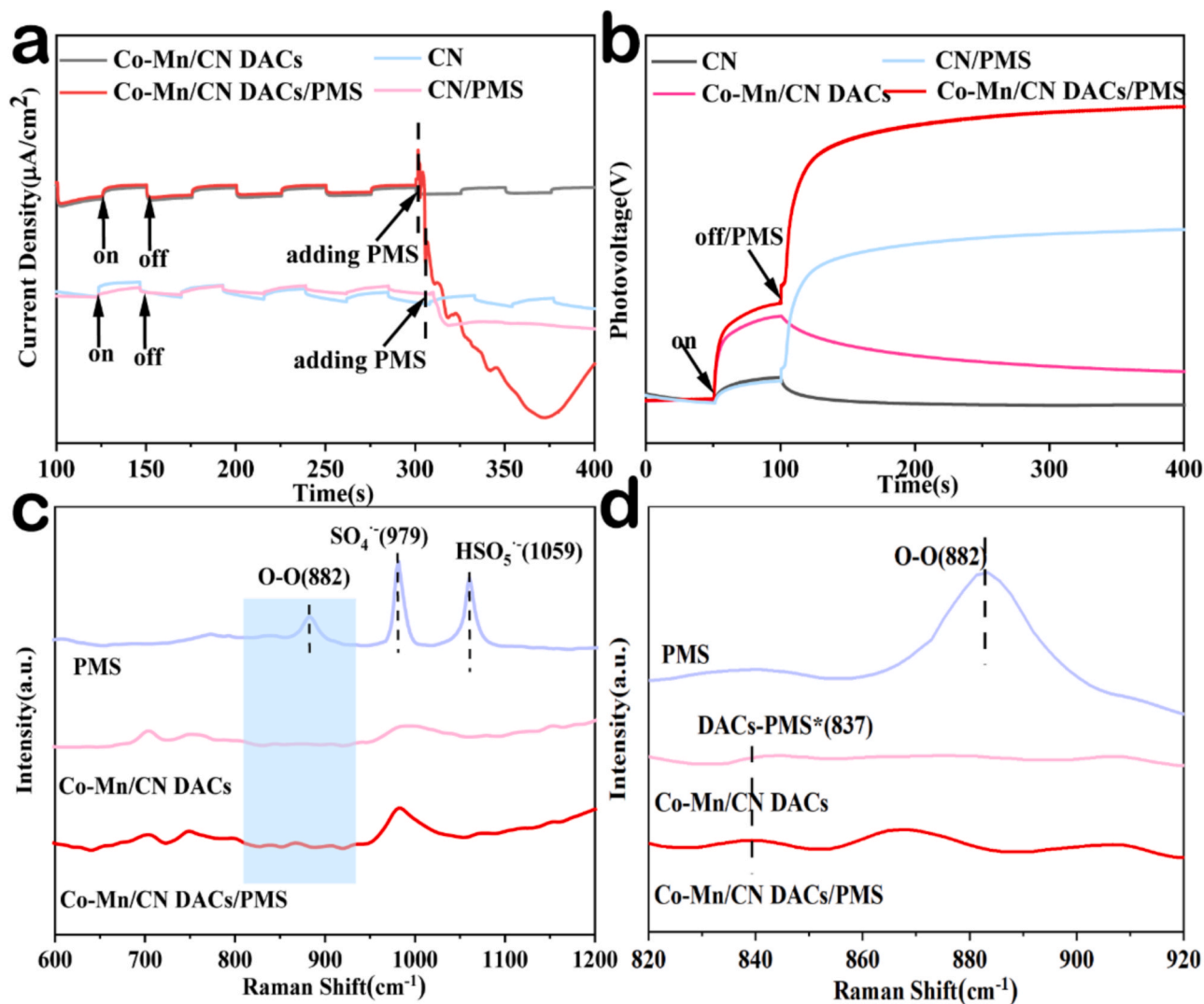


**Fig. 5.** (a) Transient photocurrent response of DACs-PMS; (b) Open-circuit voltage DACs-PMS. ([PMS]=0.4 mmol) ; (c) In-situ Raman spectra; (d) Enlarged image of in-situ Raman spectra between 800~900 $cm^{-1}$.

activity because of disharmony between photocatalysis and advanced oxidation processes (Fig. 6a). Further, Mn species were introduced to modulate local electronic structure of Cobalt metal to cascade Co4-CN catalyst, Co-Mn/CN DACs exhibits the best degradation efficiency among all the binary catalysts (Fig. 6b). Simultaneously, the results of screen of catalyst were testified by change the Co addition based on a certain Mn2 amount (Fig. S9). Importantly, compared experiments have been conducted (Fig. 6c), sole PMS cannot realize the degradation of saturated petroleum hydrocarbon $C_{14}H_{30}$ and degradation ratio only reaches 7.4 % even if visible light is exerted. Comparatively, Co4-CN exhibits a little activity under visible light degradation and such performance is comparable with that of DACs catalyst/dark/PMS condition (Fig. 6c). Excitingly, such activity is sharply boosted when PMS/visible light is simultaneously acted (~59.0 %), which highlighting the roles of PMS/visible light. Correspondingly, such synergistic effect also work in Co-Mn/CN DACs system and great activity is achieved (~80 %). It should be noted that single metal decorated catalysts are all inferior than that of Co-Mn/CN DACs catalyst as shown in Fig. 6c.

A series of reaction parameters like PMS addition amount, pH and water sources etc were investigated considering promising practical application. The amount of PMS has a certain impact on the degradation efficiency (Fig. 6d), specifically catalytic activity increase with the amount of PMS and the optimal amount is determined to be 0.4 mol/L. Certain amount of PMS is beneficial for contact opportunities between catalysts and pollutants. However, excessive amount of PMS would deteriorate the degradation performance. On one hand, excessive PMS would saturate the active sites of catalysts, which lead to inferior activation kinetics of PMS. On the other hand, excessive persulfate radicals tend to be self-consumed, which lead to the deterioration of degradation reaction[45,46].

The Co-Mn/CN DACs system endure a wide range of pH variation (3−9). The degradation rate of C14 was 82.2 % when pH was 7.0. However, excessive pH value probably is averse to the PMS activation performance, the degradation efficiency of C14 was reduced to 66 % when pH was adjusted to 11.0 (Fig. 6e). On the one hand, $HSO_5^-$ was the only form of PMS at acidic and neutral pH, which changes to $SO_5^{2-}$ at alkaline pH and hence leads to the inferior degradation ratio [47]. On the other hand, excessive $OH^-$ under alkali condition would consume $SO_4^-$ to produce $\cdot HO$ (Eqs. S1-S2), whose oxidation capability is weaker than that of $SO_4^-$ as stated in introduction of this work. All in all,
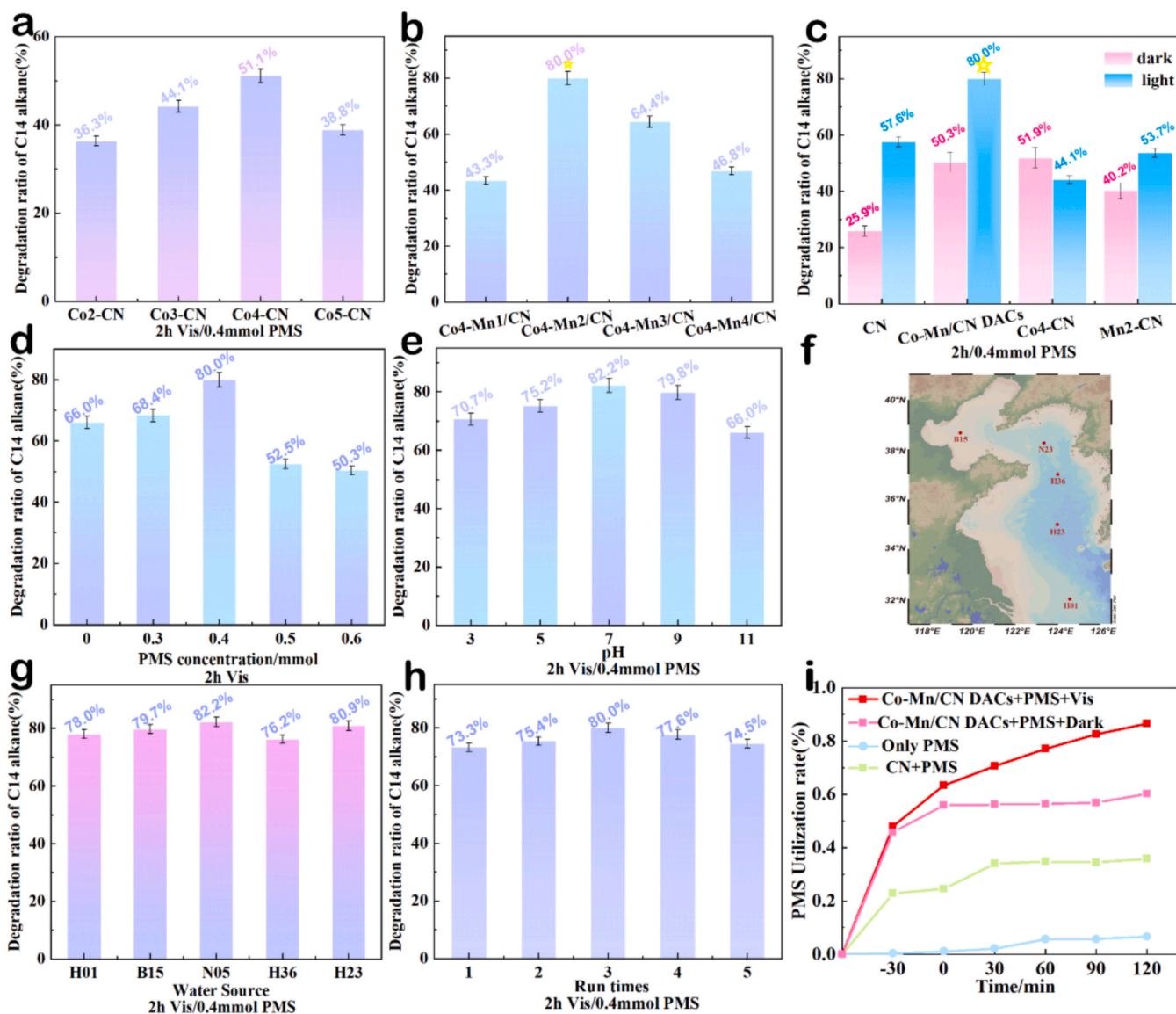


**Fig. 6.** The degradation performance of (a) Cox-CN catalysts; (b) Co4-Mnx/CN catalysts and (c) catalytic performance with or without visible light for different catalysts; (visible light illumination for 2 h, [PMS]=0.4 mmol, [Catalyst]=10 g/L, [C$_{14}$]=2 g/L, pH=7, rt). (d) PMS concentration (e) pH and (f) (g) different water source from Bohai Bay and Yellow Sea; (h) Recycle performance of Co-Mn/DACs; (i) PMS utilization ratio.
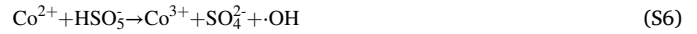
Co-Mn/CN DACs/PMS system has good pH adaptability [45].

$$SO_4^{\bullet-} + \bullet OH \rightarrow HSO_5^- + \frac{1}{2}O_2 \tag{S1}$$

$$SO_4^{\bullet-} + SO_4^{\bullet-} \rightarrow S_2O_8^{2-} \tag{S2}$$

In order to approach the practical application situation in the marine environment, the real seawater extracted from five locations in the Bohai and Yellow Seas in China is used as the water substrates polluted by petroleum hydrocarbons and the other reaction conditions remains same with above (Fig. 6f, Table. S4). As shown in Fig. 6g, Co-Mn/CN DACs exhibits superior degradation performance for petroleum hydrocarbon in the whole offshore. The degradation efficiency of C14 was still close to 80 % within 120 min after 5 runs, which all shows that Co-Mn/ CN DACs /PMS system has good recyclability and robustness (Fig. 6h). The morphology as well as structure of catalysts were evaluated after 5 times recycled using (Fig. S10). They are remain well compared to the fresh one, indicating excellent robustness in practice. More importantly, metal leaching is always a frustrating problem in AOPs, binary single metal sites performed well in recycling run due to its tough binding force with ligands. Co and Mn metal almost did not loss in recycling run (Fig. S11). Furthermore, the leaching of Co and Mn species in Co-Mn/ DACs was determined to be < 0.05 mg/L by ICP-MS, showing inferior catalytic degradation efficiency (Fig. S12). Metal leaching amount is far below that of GB 18918–2002 Discharge standard of pollutants for municipal wastewater treatment plant (Mn 2.0 mg/L), GB 3838–2002 Environmental quality standards for surface water (Co 1.0 mg/L Mn 0.1 mg/L), GB 8978–1996 Integrated wastewater discharge standard (Mn 2.0 mg/L) of china and has little impact on water environment.

The XPS of fresh and recycled Co-Mn/CN DACs were investigated to discern the roles of metal active sites. As shown in Fig. 7a, BE value of $Co^{2+}$ and $Co^{3+}$ decrease for recycled DACs, implying the local riches of electron density of Co atom. The reverse BE shift phenomenon is observed for that of Mn 2p, whose local electron density decreases (Fig. 7b). Such complementary BE shift results imply the communication of Co and Mn single metal sites (Eqs. S3, S4). More electron tends to

transfer from Mn to Co in reaction. Deeply, the peak area ratio of various metal demonstrates the ratio of $Co^{2+}$ increase and that of $Co^{3+}$ tend to decrease. Similarly, the peak area ratio of $Mn^{2+}$ increases and that of $Mn^{3+}$, $Mn^{4+}$ decreases (Fig. 7c, Table. S5). It again testifying the electron transfer effect between Co and Mn atomic sites (Eqs. S5-S11). It should be noted that the C 1s as well as N 1 s spectrum remain almost the same as that of fresh one, supporting the integrity of CN skeleton as shown in Fig. 7d-e. All in all, the recycle performance and structure of DACs assure the possibility of large-scale application in practice (Fig. 7, Fig. S10-13).

$$Mn^{2+} + Co^{3+} \rightarrow Mn^{3+} + Co^{2+} \tag{S3}$$

$$Mn^{3+} + Co^{3+} \rightarrow Mn^{4+} + Co^{2+} \tag{S4}$$

$$Co^{2+} + HSO_5^- \rightarrow Co^{3+} + SO_4^{\cdot-} + OH^- \tag{S5}$$

$$Co^{2+} + HSO_5^- \rightarrow Co^{3+} + SO_4^{2-} + \cdot OH \tag{S6}$$

$$Co^{3+} + HSO_5^- \rightarrow Co^{2+} + SO_5^{\cdot-} + H^+ \tag{S7}$$

$$Mn^{2+} + HSO_5^- \rightarrow Mn^{3+} + SO_4^{\cdot-} + OH^- \tag{S8}$$

$$Mn^{3+} + HSO_5^- \rightarrow Mn^{4+} + SO_4^{\cdot-} + OH^- \tag{S9}$$

$$Mn^{3+} + HSO_5^- \rightarrow Mn^{2+} + SO_5^{\cdot-} + H^+ \tag{S10}$$

$$Mn^{4+} + HSO_5^- \rightarrow Mn^{3+} + SO_5^{\cdot-} + H^+ \tag{S11}$$

### 3.4. Active radicals and non-radicals species and PMS activation path

Initially, chemical probe method is conducted to find out the ROS roles in such PMS activation process. MeOH, TBA, p-BQ, EDTA-2Na as well as FA acted as the chemical scavengers to quench $\bullet OH + SO_4^{\bullet-}$ (k(MeOH, $\bullet OH$)= $9.7 \times 10^8$ $M^{-1}s^{-1}$, k(MeOH,$SO_4^{\bullet-}$)= $3.2 \times 10^7$ $M^{-1}s^{-1}$,), $\bullet OH$(k(TBA, $\bullet OH$)= $(3.8-7.6) \times 10^8$ $M^{-1}s^{-1}$), $\bullet O_2$(k(p-BQ, $\bullet O_2^-$)= $(0.9-1.0) \times 10^9$ $M^{-1}s^{-1}$), $h^+$ radicals and $^1O_2$(k(FA, $^1O_2$)= $1.0 \times 10^9$ $M^{-1}s^{-1}$) species, respectively[48–50]. Degradation efficiency of
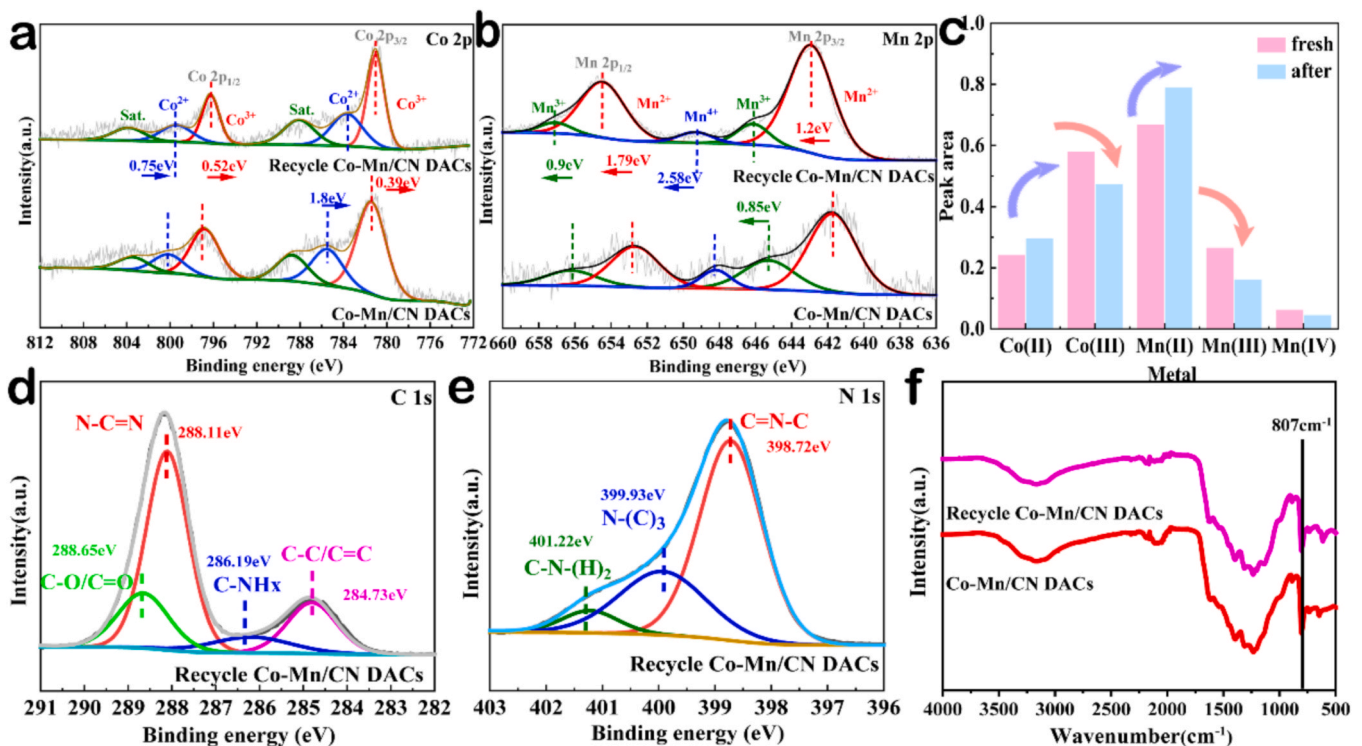


**Fig. 7.** Co 2p (a), Mn 2p (b), C1s (d) and N1s (e) XPS spectra of the corresponding catalysts; (c) Peak area of metals; (f) FTIR of fresh and recycled samples.

Co-Mn/CN DACs decreases to 61.6 %, 68.3 % and 71.6 % when 1 mmol TBA, MeOH and FA were added (Fig. 8a), implying the necessary roles of $\bullet OH$, $SO_4^{\bullet-}$ and $^1O_2$. Scavenger experiments with large number of TBA, MeOH and FA further confirmed such conclusion (Fig. S14). While $h^+$ and $\bullet O_2^-$ played minor roles in reaction process. Compared to its counterparts, apparently almost all of possible ROS and non-radicals' species have been involved into reaction process like $\bullet O_2^-$, $\bullet OH$, $SO_4^{\bullet-}$, $^1O_2$ and $h^+$. To confirm and testify such results, EPR are conducted further to identify them.

DMPO and TEMP were employed as chemical probe to combine with corresponding transient reactive species to generate EPR-responsive adducts (Fig. 8b, 8e, 8c, 8f). As shown in Fig. 8b, sole PMS system could produce trace amount of singlet oxygen $^1O_2$ under visible light illumination due to self-decomposition of PMS, but cannot generate $\bullet OH + SO_4^{\bullet-}$ whether in VL (visible light illumination) or dark conditions [51]. Comparatively, CN have enough capability to activate $HSO_5^-$ to generate $^1O_2$ as well as $\bullet OH + SO_4^{\bullet-}$ (Fig. 8c). Many researchers have

reported the superiority of g-C$_3$N$_4$ in activation of PMS driven by solar energy [52–54]. Photoexcited conduction band $e^-$ of semiconductor could transfer to surface adsorbed $HSO_5^-$ to produce $\bullet OH + SO_4^{\bullet-}$. Always there are two different mechanisms for the formation of $^1O_2$. On one hand, $HSO_5^-$ loses one electron to form $SO_5^{\bullet-}$, and two $SO_5^{\bullet-}$ further react with $H_2O$ to form $2HSO_4^-$ and $1.5\ ^1O_2$, on the other hand, $\bullet O_2^-$ formed by single electron reduction of $O_2$ in photocatalysis system could be oxidized by valence band $h^+$ to generate $^1O_2$. It is speculated the $^1O_2$ formation path of CN belongs to the latter because almost there isn't any change for $^1O_2$ signal for Co-Mn/CN DACs under VL irradiation (Fig. 8e), which implying it may not be related to PMS. Excitingly, Co-Mn/CN DACs could generate the maximum amount of $\bullet OH + SO_4^{\bullet-}$ assist by VL (Fig. 8f), which is attributed to synergistic effect of electron shuttle of DACs and enhanced adsorption behavior of PMS in DACs. Simultaneously, DACs possess both paths of $^1O_2$ formation compared to that of CN. Consistently, reaction atmosphere either supports the conclusion above. As shown in Fig. S15, different reaction atmosphere has impact
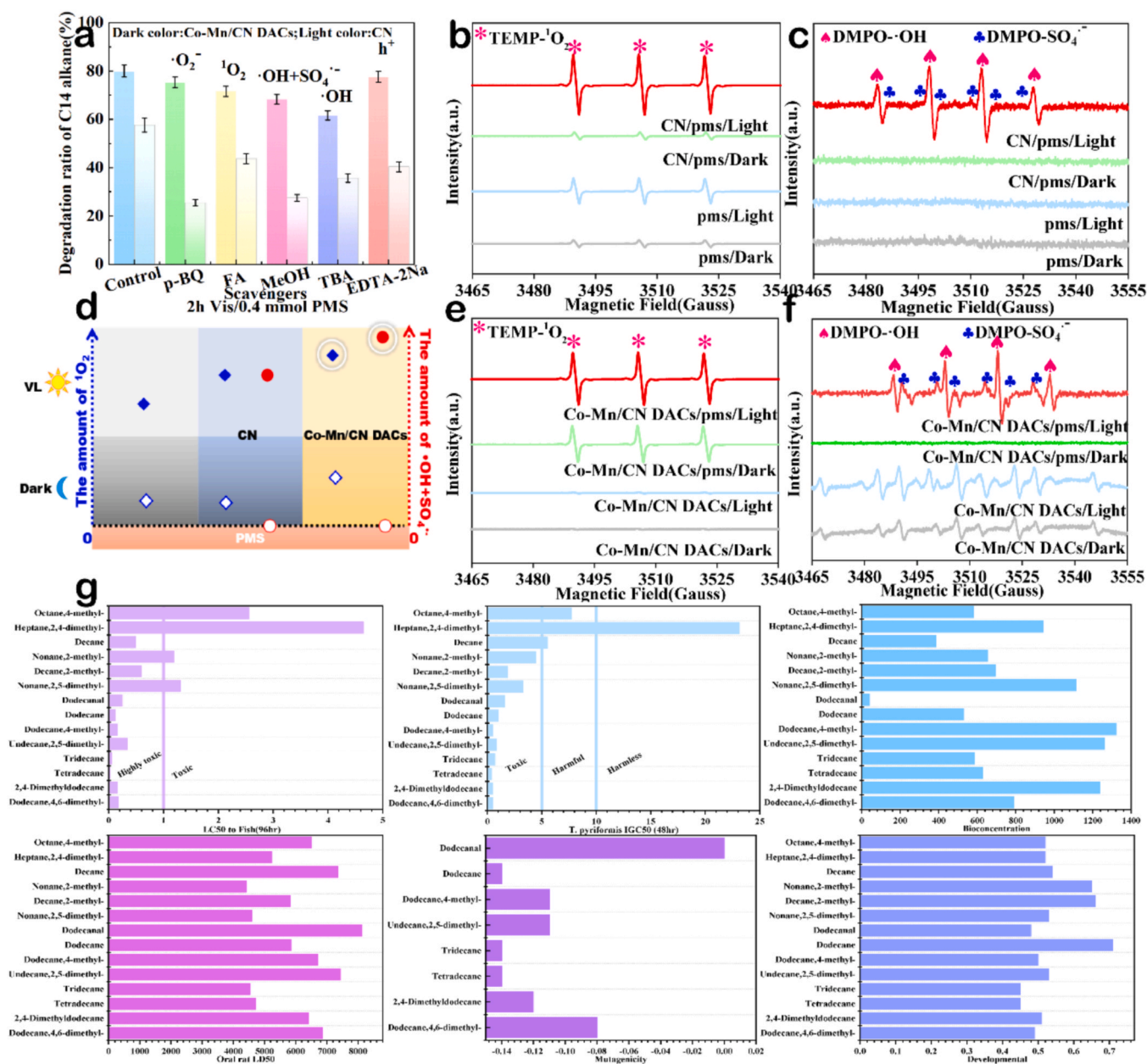


**Fig. 8.** (a) Effect of Scavengers on catalytic activity; (b) (c) (e) (f) EPR results; (d) Scheme of active species of corresponding catalysts; (g) Calculated toxicity evaluation of degradation intermediates for DACs.

on the catalytic degradation activity of DACs. Faint loss of catalytic activity have been obverted, since type of $O_2$ mediate reaction is singlet oxygen $^1O_2$ rather than $\bullet O_2^-$ for DACs, absence of oxygen molecule cutting off path IV of $^1O_2$, fortunately main formation mechanism of $^1O_2$ in Co-Mn/DACs is ascribed to path III: PMS acts as electron donor to generate $^1O_2$, therefore the absence of $O_2$ would deteriorate the degradation efficiency of organics but the extent is small because the contribution of path IV is limited. What's more, $^1O_2$ could be generated in dark for DACs compared to sole PMS as well as CN+PMS system, which may be ascribed to above mentioned $SO_5^{\bullet-}$ process [55]. Overall, the maximum amount of $\bullet OH + SO_4^{\bullet-}$ as well as $^1O_2$ under visible light illumination contribute to the removal of organic pollutant efficiently (Fig. 8d).

As we all known the first principle of remediation technology is that it should not interfere with marine ecological environment [56]. Therefore, the Calculated Toxicity of intermediates during the reaction were evaluated with the assistance of Ecological Structural Activity Relationship (ECOSAR) by the US EPA (Environmental Protection Agency). LC50 to Fish (96 hr), LC50 to Daphnid (48 hr), T. pyriformis IGC50 (48 hr), Bioconcentration, Developmental, Mutagenicity and Oral The rat LD50 toxicity index is shown in Fig. 8g, Fig. S16, Table. S6, S7. The primary pollutant $C_{14}H_{30}$ has strong toxicity to marine organisms, while acute and chronic toxicity of short-chain intermediates like $C_{12}H_{26}$, $C_{11}H_{24}$, $C_{10}H_{22}$ and $C_9H_{20}$ become weak compared to its parental counterparts. Particularly, the acute toxicity of $C_9H_{20}$ to LC50 to Daphnid (48 hr) was 1.17 mg/L, whose toxicity have been reduced much compare to its parent counterpart. What makes more sense is that some intermediates such as $C_{12}H_{24}O$ are much less toxic. The above toxicity assessment results ensure the ecological friendliness of Co-Mn/CN DACs for marine ecological environment.

To further understand the underlying mechanisms for the activation processes of PMS on Co-Mn/CN DACs, density functional theory (DFT) calculations were implemented. Firstly, all possible Co-Mn sites in $C_3N_4$ are considered, the results revealed that the Co and Mn prefer to bond
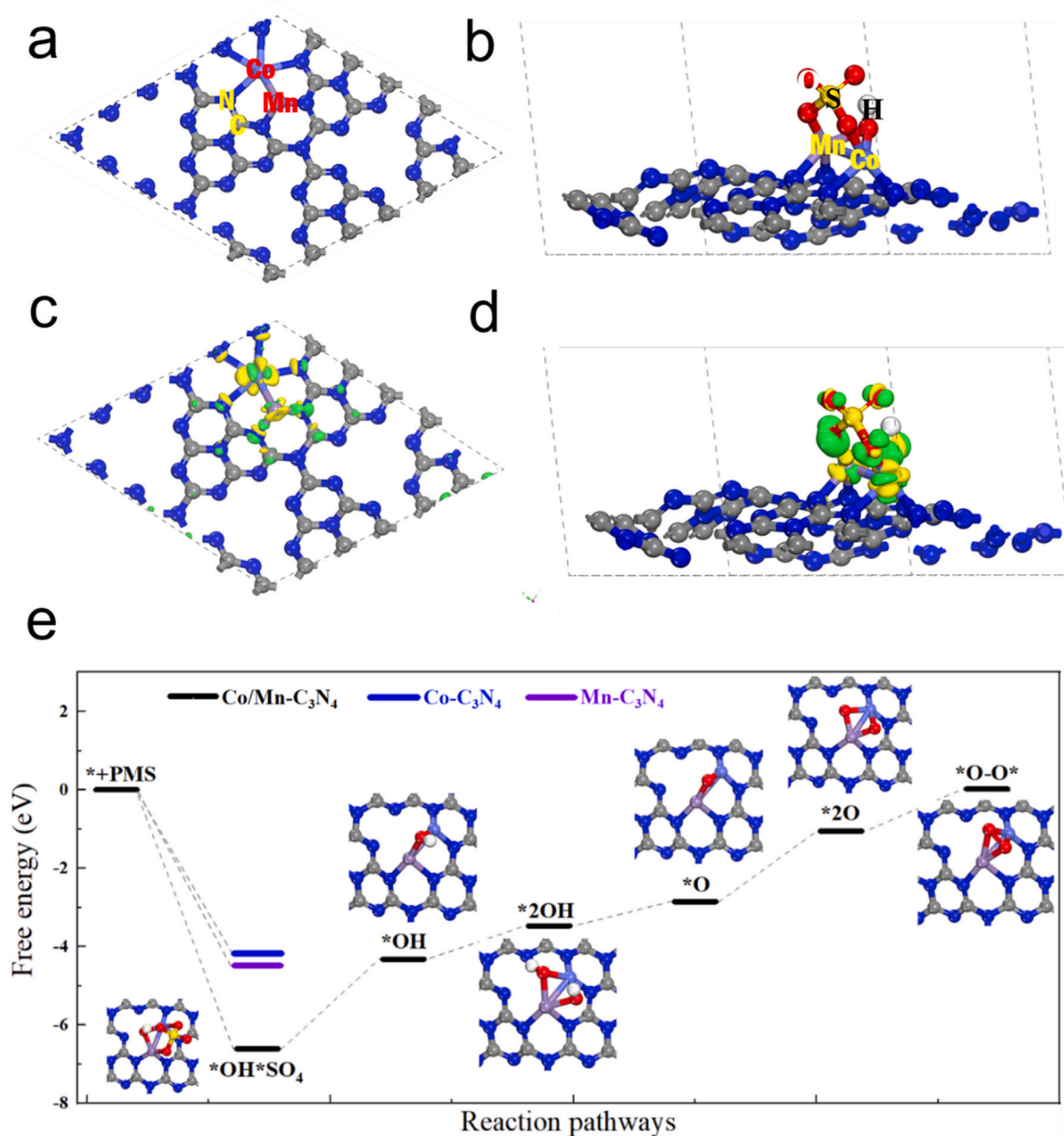


**Fig. 9.** The most stable atomic structures and the corresponding charge density differences for (a)(c) Co/Mn-doped $C_3N_4$, and (b)(d) the PMS adsorbed on Co-Mn/CN DACs, respectively. Green and yellow regions represent the electron accumulation and depletion, respectively. (e) The changes in the Gibbs free energies for the evolution processes of PMS on Co/Mn-doped $C_3N_4$. The first-step evolution process of PMS on Co- and Mn-doped $C_3N_4$ are also included as the comparison.

together, and they tend to coordinate with four and two N atoms, respectively, as shown in Fig. 9a, Fig. S17-19. Such structural information is consistent with EXAFs experimental results as have been mentioned above. As a comparison, we also considered the doping of Co and Mn in different vacancy-sites in $C_3N_4$, respectively. The most stable structure is shown in Fig. S18, it is found that such structure is only energetically 0.05 eV more stable than Co-Mn co-doped $C_3N_4$ (Fig. 9a). This result implies that the Co-, Mn-doped, and Co-Mn co-doped $C_3N_4$ structures may coexist in the experiment, while their catalytic activities must be different in view of the various coordination environment of metal atoms. In this regard, we next examined the adsorption behaviors of PMS on all these systems.

In the case of Co-Mn co-doped $C_3N_4$, all the possible adsorption sites have been considered, and the most favorable adsorption structure is shown in Fig. 9b. When PMS approaches the Co-Mn/CN DACs surface, it undergoes an automatic splitting into $SO_4$ and OH groups, accompanied by the obvious decrease in Gibbs free energy (*G*) of 6.57 eV. Next, to understand the electron transfer behavior in Co/Mn co-doped $C_3N_4$ without and with the PMS adsorption, the charge density differences were calculated as shown in Figs. 9c and 9d, in which green and yellow regions represent the electron accumulation and depletion, respectively. In the case of Co/Mn co-doped $C_3N_4$ (Fig. 9c), Mn and Co mainly donated electrons to their adjacent N atoms in $C_3N_4$. The Bader charge analysis revealed that the Mn lose more electrons (0.75 e) than that of Co (0.60 e). After the adsorption of PMS (Fig. 9d), electrons on Mn and Co were redistributed into both PMS and $C_3N_4$. In detail, Mn and Co donated 1.29 and 0.99 electrons, respectively, and a considerable number of these electrons were transferred to the PMS (1.75 e), while the others were transferred to the $C_3N_4$ (0.53 e). It is noteworthy that small electron accumulation (green) regions can also be found on both Co and Mn, indicating that a few electrons on PMS were transferred to the empty $3d$ orbitals of metal. This electron-donating/accepting phenomenon is advantageous for catalyzing the activation of PMS. Based on the above discussions, we can present the electron transfer picture on the considered system. In this picture, both Co and Mn can be viewed as electron donors, which donate significantly more electrons to PMS compared to $C_3N_4$. In particular, Mn exhibits a strong electron donating ability as compare with Co, suggesting its high catalytic activity toward PMS, which also could find evidences in the subsequent discussions utilizing the d-band center theory. It is noted that, according to Lin et al.'s very recent study[57], the huge energy release at the first decomposed step of PMS (with the formation of $SO_4^{\bullet}$ and ●OH group) on Co-Mn/CN DACs is very crucial to trigger its subsequent evolution toward $^1O_2$. To confirm this point, we have theoretically explored the activation process of PMS to $^1O_2$ which has been suggested by Lin et al.'s study [57], i.e., * + PMS → *OH*$SO_4$ → *OH → 2*OH → *O → 2*O → *O-O* → $^1O_2$, where * represents the Co-Mn/CN DACs catalyst. The detailed reaction mechanisms could be found in the Supporting Information S2.3. The changes in the Gibbs free energies (Δ*G*) for each elementary step are shown in Fig. 9e, the insets show the corresponding intermediates. It can be seen that the rate limiting process is the release of $SO_4^{\bullet}$ from the Co-Mn/CN DACs surface, with the Δ*G* values of 2.29 eV. More importantly, the significant energy release (6.57 eV) during the initial decomposition process of PMS plays a crucial role in triggering the subsequent evolution of PMS into $^1O_2$.

Based on the results above, we next calculated the Δ*G* values for the initial decomposition process of PMS on Co- and Mn-doped $C_3N_4$, respectively. As shown in Fig. 9e, the energy releases for such two processes are 4.19 and 4.56 eV, respectively, both of which are obviously lower than that of Co-Mn co-doped $C_3N_4$ (6.57 eV). The corresponding charge transfers from catalyst to $HSO_5$ in the cases of Co (1.41 e) and Mn (1.70 e) doped $C_3N_4$ are also lower than that of Co-Mn co-doped $C_3N_4$ (1.75 e). Accordingly, we could infer that, among all the considered systems, the $C_3N_4$ with the co-doping of Co-Mn plays the most import role in catalyzing the PMS, since it could strongly adsorb and decompose PMS, and eventually leading to the generation of $^1O_2$.

Next, let's discuss the intrinsic activation mechanism for the Co-Mn co-doped $C_3N_4$ towards PMS. In doing so, the partial density of states for the adsorption of PMS on Co-, Mn-doped, and Co-Mn co-doped $C_3N_4$ were calculated as shown in Fig. 10. The results revealed that the overlap between the metal-$3d$ and O-$2p$ states in Co-Mn co-doped $C_3N_4$ are enhanced as compared with the cases in Co- and Mn-doped $C_3N_4$, which further confirms the strong adsorption strength of PMS on diatomic site. It is known that the d-band center ($\mathcal{E}_d$) of metal has been widely used to describe the catalytic ability of material. In this regard, the position of $\mathcal{E}_d$ for metal-$3d$ states in all the considered systems were labeled as shown in Fig. 10. It is found that the $\mathcal{E}_d$ value of Mn-$3d$ (−1.08 eV) is higher than that of Co-$3d$ (−1.96 eV), indicating the high catalytic activity of Mn than Co, which is consistent with the relatively strong adsorption strength of PMS on Mn-doped $C_3N_4$ as has been mentioned above. Interestingly, as compared with Co- and Mn-doped $C_3N_4$, the $\mathcal{E}_d$ values for both Mn-$3d$ (−0.67 eV) and Co-$3d$ (−1.44 eV) states in the case of Co-Mn co-doped $C_3N_4$ upshifted toward the Fermi level. This means that the coupling between Co and Mn could synergistically enhance both of their catalytic activities. In particular, $\mathcal{E}_d$ value of Mn-$3d$ is obviously closer to the Fermi level than that of Co-$3d$, and the overlap between Mn-$3d$ and O-$2p$ near the Fermi level is more significant than that of Co-$3d$ and O-$2p$, both these evidences indicate the even higher chemical reactivity of Mn than Co in Co-Mn co-doped $C_3N_4$. Based on the theoretical results mentioned above, we conclude that the Co-Mn co-doped $C_3N_4$ structure is responsible for the effective evolution of PMS to $^1O_2$, and the Co-Mn coupling synergistically enhances the catalytic activities of both metals, with Mn exhibiting the superior reactivity compared to Co.

## 4. Conclusion

In summary, the binary atom active sites anchored in the visible light responsive carbon nitride Co-Mn/CN catalyst is typically designed in this work, which provides valuable information for the reasonable regulation of the diatomic site in fenton-like photocatalysts. Synchrotron radiation and theoretical calculation elucidates the coordination environment of the metal core atom, and confirms its $CoN4$-$MnN2$ part. Co-Mn/CN DACs can effectively activate PMS to degrade C14 with or without visible light illumination, and utilization rate of PMS achieves 86.5 %. Simultaneously, catalytic activity of Co-Mn/CN DACs was evaluated in various environments, which showed stable performance for degradation of C14 in oil-contaminated water under various environment. Electrochemical studies and PL characterization results confirm electron transfer in Co-Mn/CN DACs /PMS system. EPR and quenching experiments confirmed that ●OH、$SO_4^{\bullet}$ and $^1O_2$ were main radical as well as non-radicals species in the catalytic system. It also shows that the most reasonable reaction way to generate singlet oxygen species is * + PMS → *OH*$SO_4$ → *OH → 2*OH → *O → 2*O → *O-O* → $^1O_2$ by DFT calculation. This work not only provides profound guidance for the rational regulation of diatomic sites in Fenton-like catalysts, but also explains the catalytic mechanism of all-weather activation of PMS for the degradation of petroleum hydrocarbons in spilled water at the atomic scale.

## CRediT authorship contribution statement

**Qi Guo:** Experiments, Data curation, Formal analysis, Writing - Original Draft; **Xue-fang Yu:** Calculations, Writing - Review & Editing; **Kaisheng Zhang**: Calculations, Writing - Review & Editing; **Linhong Xia:** Formal analysis, Writing - Review & Editing; **Senmiao Liu:** Data curation, Formal analysis; **Weilong Zhang:** Resources, Writing-review&editing; **Yujie Du:** Data curation, Writing - Review & Editing; **Hua Tang:** Formal analysis, Writing - Review & Editing; **Yanhua Peng**: Formal analysis, Writing - Review & Editing; **Zhuo Li:** Methodology, Formal analysis, Writing - Review & Editing; **Liqin Duan** : Methodology, Formal analysis, Writing - Review & Editing; **Xiaolong Yang:**
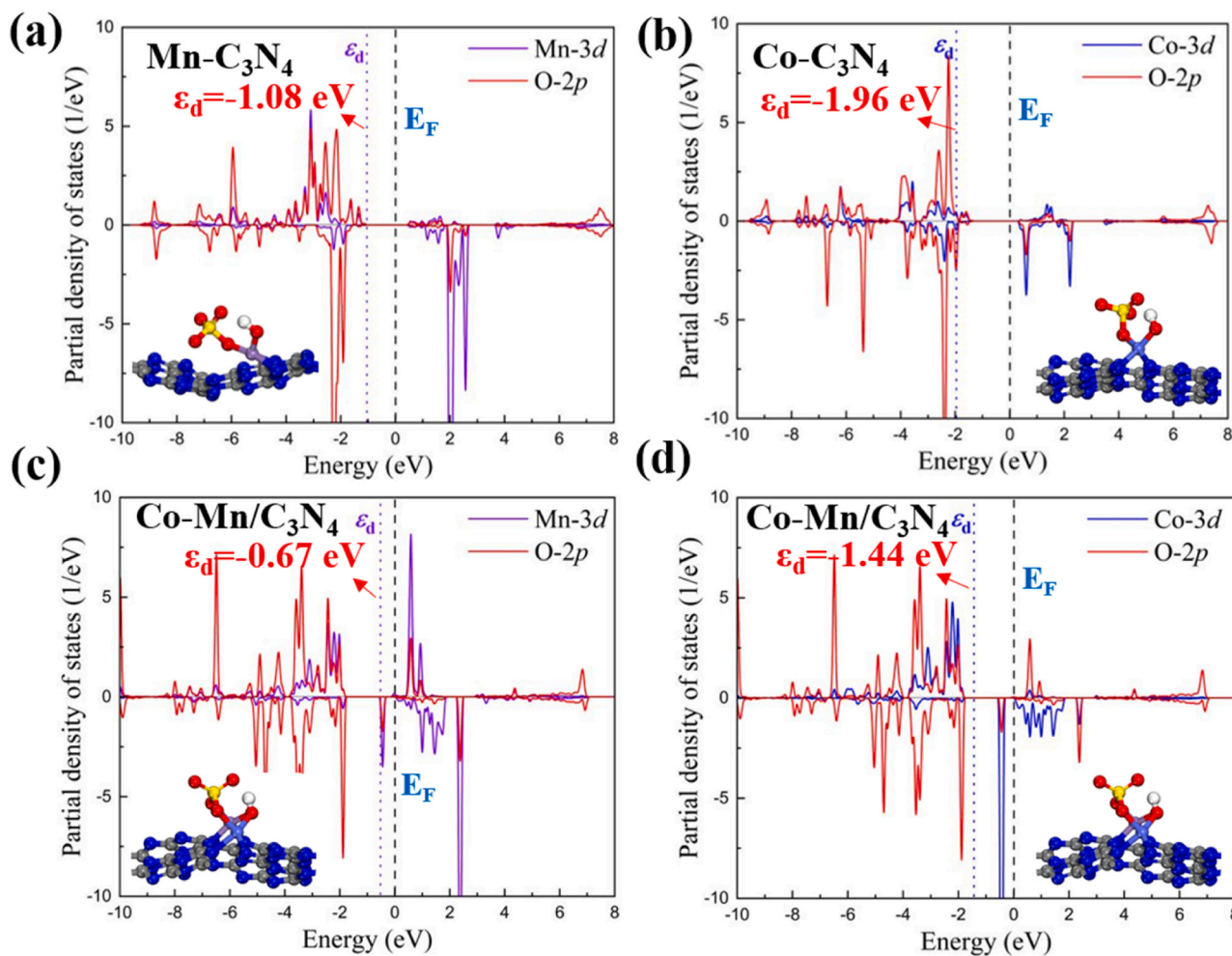
**Fig. 10.** The partial density of states and the corresponding structures for the adsorption of PMS on (a) Mn-, (b) Co-, and (c)(d) Co-Mn co-doped $C_3N_4$. Fermi level was shifted to 0 eV. $\varepsilon_d$ represents the position of d-band center of metal-$3d$ states.

Conceptualization, Methodology, Formal analysis, Funding acquisition, Supervision, Writing-review&editing.

### Declaration of Competing Interest

The authors declare that they have no known competing financial interests or personal relationships that could have appeared to influence the work reported in this paper.

### Data availability

Data will be made available on request.

### Acknowledgements

### Appendix A. Supporting information

Supplementary data associated with this article can be found in the online version at doi:10.1016/j.apcatb.2023.123581.

### References

[1] M. Yang, B. Zhang, X. Chen, Q. Kang, B. Gao, K. Lee, B. Chen, Transport of microplastic and dispersed oil co-contaminants in the marine environment, Environ. Sci. Technol. 57 (2023) 5633–5645, https://doi.org/10.1021/acs.est.2c08716.

[2] A.J. Pete, B. Bharti, M.G. Benton, Nano-enhanced bioremediation for oil spills: a review, ACS EST Eng. 1 (2021) 928–946, https://doi.org/10.1021/acsestengg.0c00217.

[3] K. Li, H. Yu, J. Yan, J. Liao, Analysis of offshore oil spill pollution treatment technology, IOP Conf. Ser.: Earth Environ. Sci. 510 (2020), https://doi.org/10.1088/1755-1315/510/4/042011.

[4] A.H.S. Solberg, Remote sensing of ocean oil-spill pollution, Proc. IEEE 100 (2012) 2931–2945, https://doi.org/10.1109/jproc.2012.2196250.

[5] Y. Wei, J. Miao, J. Ge, J. Lang, C. Yu, L. Zhang, P.J.J. Alvarez, M. Long, Ultrahigh peroxymonosulfate utilization efficiency over CuO nanosheets via heterogeneous Cu(III) formation and preferential electron transfer during degradation of phenols, Environ. Sci. Technol. 56 (2022) 8984–8992, https://doi.org/10.1021/acs.est.2c01968.

[6] J. Wang, S. Wang, Activation of persulfate (PS) and peroxymonosulfate (PMS) and application for the degradation of emerging contaminants, Chem. Eng. J. 334 (2018) 1502–1517, https://doi.org/10.1016/j.cej.2017.11.059.

[7] P. Gan, Z. Zhang, Y. Hu, Y. Li, J. Ye, M. Tong, J. Liang, Insight into the role of Fe in the synergetic effect of persulfate/sulfite and $Fe_2O_3@g$-$C_3N_4$ for carbamazepine degradation, Sci. Total Environ. 819 (2022), 152787, https://doi.org/10.1016/j.scitotenv.2021.152787.

[8] P. Liu, J. Yan, H. Huang, W. Song, Cu/Co bimetallic conductive MOFs: electronic modulation for enhanced nitrate reduction to ammonia, Chem. Eng. J. 466 (2023), https://doi.org/10.1016/j.cej.2023.143134.

[9] J. Liu, Z. Li, M. Wang, C. Jin, J. Kang, Y. Tang, S. Li, Eu₂O₃/Co₃O₄ nanosheets for levofloxacin removal via peroxymonosulfate activation: performance, mechanism and degradation pathway, Sep. Purif. Technol. 274 (2021), https://doi.org/10.1016/j.seppur.2021.118666.

[10] T. Li, M. Li, J. Jiang, Z. Zhao, Z. Li, C. Zhao, X. Wang, S. Dong, Bimetallic (Cu, Zn) ZIF-derived S-scheme heterojunction for efficient remediation of aqueous pollutants in visible light/peroxymonosulfate system, Appl. Catal. B 330 (2023), https://doi.org/10.1016/j.apcatb.2023.122539.

[11] Z. Wu, Z. Tong, Y. Xie, H. Sun, X. Gong, P. Qin, Y. Liang, X. Yuan, D. Zou, L. Jiang, Efficient degradation of tetracycline by persulfate activation with Fe, Co and O co-doped g–C₃N₄: performance, mechanism and toxicity, Chem. Eng. J. 434 (2022), https://doi.org/10.1016/j.cej.2022.134732.

[12] X. Zhang, B. Xu, S. Wang, X. Li, C. Wang, B. Liu, F. Han, Y. Xu, P. Yu, Y. Sun, Tetracycline degradation by peroxymonosulfate activated with CoNx active sites: performance and activation mechanism, Chem. Eng. J. 431 (2022), https://doi.org/10.1016/j.cej.2021.133477.

[13] C.B. Ma, Y. Xu, L. Wu, Q. Wang, J.J. Zheng, G. Ren, X. Wang, X. Gao, M. Zhou, M. Wang, H. Wei, Guided synthesis of a Mo/Zn dual single-atom nanozyme with synergistic effect and peroxidase-like activity, Angew. Chem. Int. Ed. Engl. 61 (2022), e202116170, https://doi.org/10.1002/anie.202116170.

[14] Z. Zhao, M. Hu, T. Nie, W. Zhou, B. Pan, B. Xing, L. Zhu, Improved electronic structure from spin-state reconstruction of a heteronuclear Fe-Co diatomic pair to boost the fenton-like reaction, Environ. Sci. Technol. 57 (2023) 4556–4567, https://doi.org/10.1021/acs.est.2c09336.

[15] Y. Shi, Z.R. Ma, Y.Y. Xiao, Y.C. Yin, W.M. Huang, Z.C. Huang, Y.Z. Zheng, F.Y. Mu, R. Huang, G.Y. Shi, Y.Y. Sun, X.H. Xia, W. Chen, Electronic metal-support interaction modulates single-atom platinum catalysis for hydrogen evolution reaction, Nat. Commun. 12 (2021), 3021, https://doi.org/10.1038/s41467-021-23306-6.

[16] A. Beniya, S. Higashi, Towards dense single-atom catalysts for future automotive applications, Nat. Catal. 2 (2019) 590–602, https://doi.org/10.1038/s41929-019-0282-y.

[17] X. Cui, W. Li, P. Ryabchuk, K. Junge, M. Beller, Bridging homogeneous and heterogeneous catalysis by heterogeneous single-metal-site catalysts, Nat. Catal. 1 (2018) 385–397, https://doi.org/10.1038/s41929-018-0090-9.

[18] X. Li, X. Huang, S. Xi, S. Miao, J. Ding, W. Cai, S. Liu, X. Yang, H. Yang, J. Gao, J. Wang, Y. Huang, T. Zhang, B. Liu, Single cobalt atoms anchored on porous N-doped graphene with dual reaction sites for efficient fenton-like catalysis, J. Am. Chem. Soc. 140 (2018) 12469–12475, https://doi.org/10.1021/jacs.8b05992.

[19] X. Mi, P. Wang, S. Xu, L. Su, H. Zhong, H. Wang, Y. Li, S. Zhan, Almost 100% peroxymonosulfate conversion to singlet oxygen on single-atom CoN(2+2) sites, Angew. Chem. Int. Ed. Engl. 60 (2021) 4588–4593, https://doi.org/10.1002/anie.202014472.

[20] Z. Wang, E. Almatrafi, H. Wang, H. Qin, W. Wang, L. Du, S. Chen, G. Zeng, P. Xu, Cobalt single atoms anchored on oxygen-doped tubular carbon nitride for efficient peroxymonosulfate activation: simultaneous coordination structure and morphology modulation, Angew. Chem. Int. Ed. Engl. 61 (2022), e202202338, https://doi.org/10.1002/anie.202202338.

[21] F. Huang, M. Peng, Y. Chen, X. Cai, X. Qin, N. Wang, D. Xiao, L. Jin, G. Wang, X. D. Wen, H. Liu, D. Ma, Low-temperature acetylene semi-hydrogenation over the Pd₁-Cu₁ dual-atom catalyst, J. Am. Chem. Soc. 144 (2022) 18485–18493, https://doi.org/10.1021/jacs.2c07208.

[22] Y. Zhao, H. Wu, Y. Wang, L. Liu, W. Qin, S. Liu, J. Liu, Y. Qin, D. Zhang, A. Chu, B. Jia, X. Qu, M. Qin, Sulfur coordination engineering of molybdenum single-atom for dual-functional oxygen reduction/evolution catalysis, Energy Stor. Mater. 50 (2022) 186–195, https://doi.org/10.1016/j.ensm.2022.05.015.

[23] F. Kong, R. Si, N. Chen, Q. Wang, J. Li, G. Yin, M. Gu, J. Wang, L.-M. Liu, X. Sun, Origin of hetero-nuclear Au-Co dual atoms for efficient acidic oxygen reduction, Appl. Catal. B 301 (2022), https://doi.org/10.1016/j.apcatb.2021.120782.

[24] L. Bai, C.S. Hsu, D.T.L. Alexander, H.M. Chen, X. Hu, A cobalt-iron double-atom catalyst for the oxygen evolution reaction, J. Am. Chem. Soc. 141 (2019) 14190–14199, https://doi.org/10.1021/jacs.9b05268.

[25] F.-X. Wang, Z.-W. Zhang, F. Wang, Y. Li, Z.-C. Zhang, C.-C. Wang, B. Yu, X. Du, P. Wang, H. Fu, C. Zhao, Fe-Cu bimetal metal-organic framework for efficient decontamination via Fenton-like process: synthesis, performance and mechanism, J. Colloid Interface Sci. 649 (2023) 384–393, https://doi.org/10.1016/j.jcis.2023.06.083.

[26] F. Wang, Y. Gao, H. Fu, S.-S. Liu, Y. Wei, P. Wang, C. Zhao, J.-F. Wang, C.-C. Wang, Almost 100% electron transfer regime over Fe–Co dual-atom catalyst toward pollutants removal: regulation of peroxymonosulfate adsorption mode, Appl. Catal. B 339 (2023), https://doi.org/10.1016/j.apcatb.2023.123178.

[27] J. Yang, D. Zeng, J. Li, L. Dong, W.-J. Ong, Y. He, A highly efficient Fenton-like catalyst based on isolated diatomic Fe-Co anchored on N-doped porous carbon, Chem. Eng. J. 404 (2021), https://doi.org/10.1016/j.cej.2020.126376.

[28] D. Chinnadurai, R. Rajendiran, O.L. Li, K. Prabakar, Mn-Co bimetallic phosphate on electrodeposited PANI nanowires with composition modulated structural morphology for efficient electrocatalytic water splitting, Appl. Catal. B 292 (2021), https://doi.org/10.1016/j.apcatb.2021.120202.

[29] A. Sampath, T. Ricciardulli, P. Priyadarshini, R. Ghosh, J.S. Adams, D.W. Flaherty, Spectroscopic evidence for the involvement of interfacial sites in O–O bond activation over gold catalysts, ACS Catal. 12 (2022) 9549–9558, https://doi.org/10.1021/acscatal.2c02076.

[30] X.-P. Zhang, H.-Y. Wang, H. Zheng, W. Zhang, R. Cao, O–O bond formation mechanisms during the oxygen evolution reaction over synthetic molecular catalysts, Chin. J. Catal. 42 (2021) 1253–1268, https://doi.org/10.1016/s1872-2067(20)63681-6.

[31] H. Wang, W. Xu, X. Chen, Q. Yang, C. Shen, B. Zhang, Y. Lin, J. Sun, L. Zhang, Q. Zhang, Z. Lu, L. Chen, Transformation from a non-radical to a radical pathway via the amorphization of a Ni(OH)₂ catalyst as a peroxymonosulfate activator for the ultrafast degradation of organic pollutants, Nanoscale 13 (2021) 7700–7708, https://doi.org/10.1039/d1nr00933h.

[32] W. Wang, Q. He, Y. Yi, Y. Xiao, X. Xiao, H. Yang, X. Dong, Boosting piezocatalytic activity of graphitic carbon nitride for degrading antibiotics through morphologic regulation and chlorine doping, J. Clean. Prod. 415 (2023), https://doi.org/10.1016/j.jclepro.2023.137818.

[33] L. Xia, K. Zhang, X. Wang, Q. Guo, Y. Wu, Y. Du, L. Zhang, J. Xia, H. Tang, X. Zhang, Y. Peng, Z. Li, X. Yang, 0D/2D Schottky junction synergies with 2D/2D S-scheme heterojunction strategy to achieve uniform separation of carriers in 0D/2D/2D quasi CNQDs/TCN/ZnIn₂S₄ towards photocatalytic remediating petroleum hydrocarbons polluted marine, Appl. Catal. B 325 (2023), https://doi.org/10.1016/j.apcatb.2023.122387.

[34] P. Niu, L. Li, Overall photocatalytic water splitting of crystalline carbon nitride with facet engineering, Chem 6 (2020) 2439–2441, https://doi.org/10.1016/j.chempr.2020.09.009.

[35] P. Kagioulis, R. Ramesh, M. van Goethem, M. Saric, Y.C. van Delft, Heat-integrated distillation columns as a retrofit cannot bring energy savings to the ethylene plant, Ind. Eng. Chem. Res. 60 (2021) 7342–7351, https://doi.org/10.1021/acs.iecr.1c00500.

[36] L. Xia, Z. Sun, Y. Wu, X.-F. Yu, J. Cheng, K. Zhang, S. Sarina, H.-Y. Zhu, H. Weerathunga, L. Zhang, J. Xia, J. Yu, X. Yang, Leveraging doping and defect engineering to modulate exciton dissociation in graphitic carbon nitride for photocatalytic elimination of marine oil spill, Chem. Eng. J. 439 (2022), https://doi.org/10.1016/j.cej.2022.135668.

[37] S. Yang, Y. Gong, J. Zhang, L. Zhan, L. Ma, Z. Fang, R. Vajtai, X. Wang, P. M. Ajayan, Exfoliated graphitic carbon nitride nanosheets as efficient catalysts for hydrogen evolution under visible light, Adv. Mater. 25 (2013) 2452–2456, https://doi.org/10.1002/adma.201204453.

[38] Q. Li, Y. He, R. Peng, Graphitic carbon nitride (g-C₃N₄) as a metal-free catalyst for thermal decomposition of ammonium perchlorate, RSC Adv. 5 (2015) 24507–24512, https://doi.org/10.1039/c5ra01157d.

[39] Y. Yao, C. Wang, Y. Yang, S. Zhang, X. Yan, C. Xiao, Y. Zhou, Z. Zhu, J. Qi, X. Sun, J. Li, Mn-Co dual sites relay activation of peroxymonosulfate for accelerated decontamination, Appl. Catal. B 330 (2023), https://doi.org/10.1016/j.apcatb.2023.122656.

[40] S. Guo, Z. Li, Y. Li, Z. Zeng, J. Lv, S. Huang, Y. Wang, X. Ma, CoMn catalysts derived from partial decomposed layered CoMn-MOF materials for higher alcohol synthesis from syngas, Chem. Eng. J. 463 (2023), https://doi.org/10.1016/j.cej.2023.142359.

[41] Y. Gao, Y. Zhu, L. Lyu, Q. Zeng, X. Xing, C. Hu, Electronic structure modulation of graphitic carbon nitride by oxygen doping for enhanced catalytic degradation of organic pollutants through peroxymonosulfate activation, Environ. Sci. Technol. 52 (2018) 14371–14380, https://doi.org/10.1021/acs.est.8b05246.

[42] J. Wang, H. Zhong, J. Yang, H. Li, P. Tang, Y. Feng, D. Li, Tuning the atomic configuration environment of MnN4 sites by Co cooperation for efficient oxygen reduction, J. Energy Chem. 82 (2023) 547–559, https://doi.org/10.1016/j.jechem.2023.04.010.

[43] J. Feng, H. Gao, L. Zheng, Z. Chen, S. Zeng, C. Jiang, H. Dong, L. Liu, S. Zhang, X. Zhang, A Mn-N3 single-atom catalyst embedded in graphitic carbon nitride for efficient CO₂ electroreduction, Nat. Commun. 11 (2020), https://doi.org/10.1038/s41467-020-18143-y.

[44] X. Liu, J. Wang, D. Wu, Z. Wang, Y. Li, X. Fan, F. Zhang, G. Zhang, W. Peng, N-doped carbon dots decorated 3D g-C₃N₄ for visible-light driven peroxydisulfate activation: insights of non-radical route induced by Na⁺ doping, Appl. Catal. B 310 (2022), https://doi.org/10.1016/j.apcatb.2022.121304.

[45] S. Xiong, H. Zeng, R. Tang, L. Li, Z. Zhou, J. Wang, C. Ding, D. Gong, Y. Deng, Synergistic effect of high-valent cobalt oxo species and piezoelectricity on enhanced peroxymonosulfate activation for atrazine removal, Chem. Eng. J. 466 (2023), https://doi.org/10.1016/j.cej.2023.143200.

[46] Y. Wang, L. Fang, Z. Wang, Q. Yang, Peroxymonosulfate activation by graphitic carbon nitride co-doped with manganese, cobalt, and oxygen for degradation of trichloroethylene: effect of oxygen precursors, kinetics, and mechanism, Sep. Purif. Technol. 278 (2021), https://doi.org/10.1016/j.seppur.2021.119580.

[47] L. Zhang, H. Zhang, J. Qi, L. Xing, Z. Fang, T. Qi, L. Wang, Boosting in-situ Fenton-like degradation on bifunctional CoFe-CoFe₂O₄@N-C via constructing "adsorption trap": Unveiling the role of pyrrolic N, Appl. Surf. Sci. 634 (2023), https://doi.org/10.1016/j.apsusc.2023.157649.

[48] S. Feijoo, X. Yu, M. Kamali, L. Appels, R. Dewil, Generation of oxidative radicals by advanced oxidation processes (AOPs) in wastewater treatment: a mechanistic, environmental and economic review, Rev. Environ. Sci. Biotechnol. 22 (2023) 205–248, https://doi.org/10.1007/s11157-023-09645-4.

[49] Y. Liu, X. Yu, M. Kamali, X. Zhang, S. Feijoo, S.M. Al-Salem, R. Dewil, L. Appels, Biochar in hydroxyl radical-based electrochemical advanced oxidation processes (eAOPs) – mechanisms and prospects, Chem. Eng. J. 467 (2023), https://doi.org/10.1016/j.cej.2023.143291.

[50] M. Zhao, X. Wang, S. Wang, M. Gao, Hydroxyl radical induced Cr flocculation via redox reaction: the extending application of heterogeneous advanced oxidation processes on Cr removal, J. Hazard. Mater. 452 (2023), 131282, https://doi.org/10.1016/j.jhazmat.2023.131282.

[51] M. Xie, J. Tang, L. Kong, W. Lu, V. Natarajan, F. Zhu, J. Zhan, Cobalt doped g-C$_3$N$_4$ activation of peroxymonosulfate for monochlorophenols degradation, Chem. Eng. J. 360 (2019) 1213–1222, https://doi.org/10.1016/j.cej.2018.10.130.

[52] B. Xu, X. Zhang, Y. Zhang, S. Wang, P. Yu, Y. Sun, X. Li, Y. Xu, Enhanced electron transfer-based nonradical activation of peroxymonosulfate by CoNx sites anchored on carbon nitride nanotubes for the removal of organic pollutants, Chem. Eng. J. 466 (2023), https://doi.org/10.1016/j.cej.2023.143155.

[53] R. Tang, H. Zeng, Y. Deng, S. Xiong, L. Li, Z. Zhou, J. Wang, L. Tang, Dual modulation on peroxymonosulfate activation site and photocarrier separation in carbon nitride for efficient photocatalytic organics degradation: efficacy and mechanism evaluation, Appl. Catal. B 336 (2023), https://doi.org/10.1016/j.apcatb.2023.122918.

[54] B. Chen, X. Liu, B. Liu, Q. Han, L. Li, L. Wang, Y. Shu, L. Zang, W. Zhu, Z. Wang, Singlet oxygen generation in light-assisted peroxymonosulfate activation by carbon nitride: role of elevated crystallinity, Chemosphere 321 (2023), 138112, https://doi.org/10.1016/j.chemosphere.2023.138112.

[55] Z. Ni, C. Zhang, H. Ma, J. Liu, Z. Wang, K. Zhu, M. Li, H. Jia, Facet-dependent photo-degradation of nitro polycyclic aromatic hydrocarbons on hematite under visible light: participation of environmentally persistent free radicals and reactive oxygen/nitrogen species, Appl. Catal. B 318 (2022), https://doi.org/10.1016/j.apcatb.2022.121816.

[56] S. Li, C. Wang, M. Cai, F. Yang, Y. Liu, J. Chen, P. Zhang, X. Li, X. Chen, Facile fabrication of TaON/Bi$_2$MoO$_6$ core–shell S-scheme heterojunction nanofibers for boosting visible-light catalytic levofloxacin degradation and Cr(VI) reduction, Chem. Eng. J. 428 (2022), https://doi.org/10.1016/j.cej.2021.131158.

[57] J. Lin, L. Jiang, W. Tian, Y. Yang, X. Duan, Y. Jiao, H. Zhang, S. Wang, The structure-dependent mechanism of single-atom cobalt on macroporous carbon nitride in (photo-)Fenton-like reactions, J. Mater. Chem. A 11 (2023) 13653–13664, https://doi.org/10.1039/d3ta01926h.